SPATIAL DETERMINANTS OF TUMOR CELL DEDIFFERENTIATION AND PLASTICITY IN PRIMARY CUTANEOUS MELANOMA

Tuulia Vallius*[1,2,3], Yingxiao Shi*[1,4], Edward Novikov*[1], Shishir M Pant[1,2,3], Roxanne Pelletier[1,2], Yu-An Chen[1], Juliann B. Tefft[1], Ajit Nirmal Johnson[1,5], Zoltan Maliga[1,2], Guihong Wan[1,6], Mia DeSimone[8], George Murphy[8], Sandro Santagata[1,2,8], Yevgeniy R Semenov[1,6], David Liu[7], Christine G Lian[8+], and Peter K Sorger[1,2,3+]

[1]Laboratory of Systems Pharmacology, Harvard Program in Therapeutic Science, Harvard Medical School, 200 Longwood Avenue, Boston, MA 02115;
[2]Ludwig Center at Harvard;
[3]Department of Systems Biology, Harvard Medical School, 200 Longwood Avenue, Boston, MA 02115.
[4]Department of Clinical Computational Oncology, Dana-Farber Cancer Institute, 450 Brookline Avenue, Boston, MA 02215;
[5]Department of Dermatology, Brigham and Women's Hospital, Harvard Medical School, 75 Francis Street, Boston, MA 02115;
[6]Department of Dermatology, Massachusetts General Hospital;
[7]Department of Medical Oncology, Dana-Farber Cancer Institute, 450 Brookline Avenue, Boston, MA 02215;
[8]Department of Pathology, Brigham and Women's Hospital, Harvard Medical School, 75 Francis Street, Boston, MA 02115

* These (co-first) authors contributed equally
[+] These senior authors contributed equally

†Corresponding Author; peter_sorger@hms.harvard.edu

Peter K. Sorger, WAB 432, Department of Systems Biology, Harvard Medical School, 200 Longwood Avenue, Boston, MA 02115.
Phone: 617-432-6901
E-mail: peter_sorger@hms.harvard.edu

RUNNING TITLE

Spatial variation and de-differentiation in primary melanoma

STATEMENT OF SIGNIFICANCE

This study shows that tumor cell dedifferentiation and plasticity are locally patterned in primary human melanomas under the influence of microenvironment components such as myeloid cells and vasculature. As a result, neighborhoods in a single tumor can be as different from each other as in different tumors.

KEYWORDS

Cutaneous melanoma, multiplex imaging, spatial transcriptomics, cancer progression, dedifferentiation, lineage plasticity, cell state switch, spatial variance, intratumor heterogeneity, melanoma heterogeneity

CONFLICT OF INTEREST

PKS is a co-founder and member of the BOD of Glencoe Software, member of the SAB for RareCyte, Reverb Therapeutics and Montai Health, and consultant for Merck; he holds equity in Glencoe and RareCyte. The other authors declare no potential conflicts of interest.

ORCID
Tuulia Vallius 0000-0002-3006-4887
Yingxiao Shi- 0000-0003-2783-9642
Edward Novikov - 0000-0003-1476-5111
Shishir Pant - 0000-0002-2686-7898
Roxanne Pelletier - 0000-0002-1957-5483
Yu-An Chen – 0000-0001-7228-4696
Ajit J. Nirmal - 0000-0003-4139-0618
Zoltan Maliga- 0000-0003-4209-7253
Guihong Wan - 0000-0003-1100-4018
Yevgeniy Semenov - 0000-0002-7387-3094
Juliann B. Tefft- 0000-0002-8826-665X
David Liu - 0000-0003-0346-5033
George Murphy- 0000-0001-9362-5146
Christine Lian- 0000-0003-4626-1612
Sandro Santagata - 0000-0002-7528-9668
Peter K Sorger - 0000-0002-3364-1838

ABSTRACT

Localized cutaneous melanoma can be cured by excision but success critically depends on early detection and risk assessment of primary lesions. However, their initiation, progression, and immunology remain poorly understood, partly due to high intra- and inter-tumor heterogeneity. We studied this heterogeneity using spatial profiling in over 300 histological domains, each representing a single progression stage, and found that 200-600 cell neighborhoods from a single melanoma can be as different in RNA and protein expression as neighborhoods from different tumors. These differences are not stochastic, however, and disease progression can be mapped at the neighborhood level onto a cell state landscape defined by the activity of the melanocyte master regulator MITF and genes associated with a dedifferentiated neural crest phenotype. Position in this landscape is influenced by proximity to immune cells, perivascular environments, and other tissue features, but no single association is absolute, giving rise to complex spatial patterns.

INTRODUCTION

Cutaneous melanoma is the most aggressive type of skin cancer: metastatic disease remains lethal in many patients, despite the approval of targeted therapies and immune checkpoint inhibitors (ICIs).[1] The incidence of cutaneous melanoma is projected to double between 2020 and 2040 due to changes in sun exposure and diagnostic criteria[2] but local surgery can be curative if the disease is detected early. Early detection is dependent on routine skin surveillance[3] followed by biopsy or excision of suspicious lesions for histopathological evaluation. This involves examination of hematoxylin and eosin (H&E) stained tissue sections prepared from formalin-fixed paraffin embedded (FFPE) specimens, complemented in some cases by immunohistochemistry (IHC) but rarely by sequencing. Decades of H&E and IHC-based histopathology have led to highly refined morphological criteria for melanoma diagnosis and staging[4] but identifying aggressive tumors remains difficult and a substantial portion of metastatic disease involves recurrence in patients who have undergone surgery with curative intent.[5] This inability to predict melanoma recurrence and the countervailing pressure to avoid overdiagnosis[6] highlights a substantial need for new approaches to predicting melanoma risk based on better understanding of cellular and molecular properties associated with progression in primary disease. Fortunately, the ready availability of FFPE specimens representing the earliest stages of melanoma and the introduction of spatial profiling methods well-suited to the limitations of these small specimens represent an excellent setting in which to study how solid tumors first arise and overcome immune surveillance.

The initiation and progression of cutaneous melanoma is a multistep molecular process[7–11] involving distinct histological stages: (i) a premalignant state (either atypical melanocytes in “precursor fields” or nevi), (ii) *melanoma in situ* (MIS), a pre-invasive state, (iii) locally invasive cancer typically exhibiting a radial growth phase followed by a deeply invasive vertical growth phase (RGP and VGP), (iv) locoregional metastasis (e.g., to draining lymph nodes), and (v) distant metastasis to the skin, brain, lungs, and liver. In some specimens, multiple stages of primary melanoma from precursor field to

104 invasive tumors can be found in a single tissue block, creating an opportunity to study progression in a
105 single individual.[12]
106
107 DNA sequencing has established an essential role for driver mutations in oncogenes such as *BRAF*,
108 *NRAS* and *KIT* during melanoma initiation and metastasis,[13–16] and single-cell sequencing and IHC have
109 demonstrated a role for lineage plasticity and tumor cell dedifferentiation in therapy resistance,
110 particularly in the metastatic setting.[17–24] MITF is a master regulator and critical factor in melanocyte
111 differentiation, melanosome formation, and melanin biosynthesis and genes controlled by *MITF* can be
112 either up- or down-regulated during melanoma progression. For example, during induction of "epithelial-
113 to-mesenchymal" transitions (EMT) in progressing melanomas, *MITF* expression decreases,[25] leading to
114 repression of transcriptional programs involved in pigment production. Inflammatory microenvironments
115 have been reported to induce cell plasticity[26–29] and a switch from *MITF*-driven melanocytic states to an
116 invasive dedifferentiated state characterized by expression of *NGFR*, *AXL*, and *SOX9*[13,18–20,30]. The
117 presence of endothelial cells is another factor proposed to contribute to dedifferentiation and melanoma
118 growth (in mouse models).[31]
119
120 Both primary and metastatic melanoma are characterized by high intra-tumoral heterogeneity[32,33] and this
121 has direct implications for the use of biomarkers in diagnosis.[34–36] Heterogeneity within a single
122 specimen[37] and across specimens of similar stages[36] in the expression of *MITF*-regulated proteins such
123 as MART1[38] and PMEL[39] or the SOX10 transcription factor[40] has made it challenging to identify a
124 definitive progression biomarker or biomarker combination. Thus, no molecular or genetic features are
125 routinely part of diagnosis in the primary disease setting. Instead, the current melanoma staging system
126 (the AJCC 8th edition for melanoma staging)[41] relies primarily on visual assessment of H&E-stained
127 sections to score the depth of invasion (the Breslow depth), presence or absence of ulceration (which
128 can also have a macroscopic presentation), and whether or not lymph node metastases are present.[4,41]
129 The presence of tumor-adjacent lymphocytes (a "brisk" TIL response)[42] is often recorded in pathology
130 reports but the prognostic significance remains uncertain.[43]
131
132 A further limitation in our understanding of primary melanomas is that molecular profiling[44] has been
133 performed primarily in metastatic disease[13,14,33], with primary disease remaining less thoroughly studied.[12]
134 In part, this is because formaldehyde fixation and small specimen size (along with a requirement to
135 preserve tissue for patients who are still alive) make traditional RNA and scRNA sequencing difficult.
136 Studies (including those from our own laboratories) on limited numbers of primary melanomas have
137 shown that EMT-like transcriptomic programs are associated with poor survival in primary melanoma[25],
138 and that de-differentiation can be observed in pre-treatment and pre-metastatic stages.[12,25,45–47] These
139 studies suggest that additional genetic and epigenetic changes found in metastatic disease might also be
140 present in primary melanoma.
141

142 In this paper we characterize inter- and intra-tumoral heterogeneity of primary melanomas at a molecular
143 level with the goal of distinguishing random variation (as observed for passenger mutations in metastatic
144 cancers)[48] from recurrent and patterned variation in over 300 distinct histological domains from 62
145 primary cutaneous melanomas. The majority of these specimens contained multiple progression stages
146 ranging from adjacent normal skin to the cutaneous component of Stage III (metastatic) melanoma.
147 Patterns of protein and gene expression were measured using cyclic multiplexed immunofluorescence
148 (CyCIF)[49] imaging and GeoMx microregional transcriptomics.[50] Confirming previous histological and IHC
149 data, we failed to identify any single protein feature predictive of disease stage and found that
150 microregions (MRs; typically 200-600 histologically similar tumor cells) from a single specimen could
151 differ from each other to as great a degree as MRs from all specimens. However, these differences were
152 not random but were instead organized spatially based on MITF activity, melanocyte dedifferentiation,
153 and other molecular features. Moreover, these features were strongly associated with the degree of local
154 inflammation and proximity to the vasculature. Thus, both inter- and intra-tumoral heterogeneity in
155 primary melanoma appear to be influenced in large part by the local microenvironment, which is in turn
156 patterned by mesoscale features such as vessels and lamina that organize normal tissue.
157
158 **RESULTS**
159 **Patient cohort and spatial data generation**
160 Archival FFPE specimens of primary cutaneous melanoma from 62 patients (**Fig. 1A,B**; MEL14 to
161 MEL86; see **Supplementary Table S1** for HTAN identifiers) were reviewed by a board-certified
162 dermatopathologist and annotated for the presence of five histological features associated with disease
163 progression: (i) adjacent normal skin, (ii) melanocytic atypia (precursor fields), (iii) melanoma in situ
164 (MIS), (iv) radial growth phase (RGP) and (v) vertical growth phase melanoma (VGP; **Fig. 1C,D;**
165 **Supplementary Fig. S1A**). Sample set A (n=45) was selected for the presence of multiple progression
166 stages within the same sample with an emphasis on stage I and set B (n=17) was selected for stage II
167 disease; multiple stages were often present in these specimens, but this was not a selection criterion.
168
169 Melanocytic nevi and *de novo* melanomagenesis from precursor fields (morphologically atypical
170 melanocytes[51]) are the two currently recognized routes to melanoma initiation[7] with current evidence
171 suggesting that nevi initiate ~20% of melanomas and precursor fields ~80%.[52,53] This study focuses on
172 the latter: precursor fields comprising discontinuous, non-pagetoid intraepidermal proliferation of
173 cytologically dysplastic melanocytes located at the perimeter of, and in contiguity with, stage 0-III
174 melanoma. Upon progression, these atypical melanocytes continuously replace the basal layer of the
175 epidermis and/or exhibit pagetoid scatter giving rise to MIS (Stage 0). Stages I & II melanoma involve
176 increasing depths of dermal invasion (Breslow depth) and Stage III includes locoregional metastasis
177 (**Supplementary Fig. S1A**).[54,55] Histopathological annotation of 62 specimens yielded a total of 313
178 distinct histological regions (HRs) each representing a different progression stage (ranging from 1 to 14

179 per specimen; average 4); these HRs were also scored for the presence of tumor infiltrating lymphocytes
180 (TILs), and for epithelioid, spindle, rhabdoid, and pleomorphic tumor cell morphologies.
181
182 We then performed 34 to 49-plex whole-slide CyCIF imaging on these specimens (**Supplementary Fig.**
183 **S1B**) and used histopathological annotations and CyCIF data to guide the selection of microregions
184 (MRs) for GeoMx microregional transcriptomic profiling. These MRs ranged in size from ~100 cells for
185 normal and precursor areas to ~350 cells for RGP and VGP regions (**Fig. 1C; Supplementary Fig.**
186 **S1C,D**) which is similar to the correlation length scales for many tumor features, as previously
187 described.[56] Prior to mRNA preparation, MRs containing a mixture of melanocyte/tumor cells and other
188 cell types were separated into tumor, non-tumor and immune compartments using either a mixture of
189 anti-SOX10 and anti-MART1 antibodies or anti-CD45 antibodies (referred to as "segmentation" in the
190 GeoMx workflow; **Supplementary Figs. S1D, S2A** and **Supplementary Table S2**); a total of 1266 MRs
191 were profiled. Archival specimens of primary melanoma can be difficult to manage when friable; thus, not
192 all specimens that generated GeoMx and CyCIF data passed quality control and could be included in the
193 final dataset (**Fig. 1B**).[57]
194
195 To identify protein features associated with melanoma initiation and progression, CyCIF images were
196 segmented using algorithms in MCMICRO[58] and marker intensities were quantified in ~2 x 10^6 tumor and
197 ~3 x 10^6 non-tumor cells followed by gating and cell type calling (see **Supplementary Fig. S2B-E** for
198 markers and cell type identification plan). Melanocytes and tumor cells were further subdivided based on
199 the expression of melanocytic lineage markers (e.g., MART1, S100A1), clinical biomarkers (e.g.,
200 PRAME), differentiation markers (e.g., SOX9, SOX10, NGFR), and proliferation markers (e.g., KI67, pH3;
201 see **Supplementary Fig. S2C** for gating strategy and **Supplementary Table S3** for index of gene and
202 protein names). The proportions of tumor cells corresponding to melanocytic, transitional, mesenchymal,
203 and neural-crest (NC) lineages were then determined based on patterns of SOX10, MART1, SOX9, and
204 NGFR marker co-expression (**Fig. 2A,B**).

205 **Association of melanocytic differentiation with progression and intertumoral heterogeneity**
206 The majority of melanocytes in normal and precursor regions were melanocytic (defined as $SOX10^+$
207 $MART1^+$, **Fig. 2A-C**, **Supplementary Fig. S3A,B, Supplementary Table S4**). Mesenchymal states
208 ($MART1^-$ and $SOX9^+$) emerged only in invasive melanomas, and de-differentiated neural-crest like tumor
209 cells ($NGFR^+$) were restricted to later progression stages (**Fig. 2A,C**). Similar trends were observed for
210 Breslow depth, a measure of the maximal depth of dermal invasion used for clinical staging
211 (**Supplementary Fig. S3C**). These results are consistent with an extensive histopathology literature
212 based on H&E staining and single channel IHC of primary melanoma.[34–36] When GeoMx transcriptomic
213 profiles from 900 tumor MRs were compared to published transcriptional signatures derived from scRNA
214 sequencing of metastatic tumors and melanoma cell lines[26,59,60], a good correspondence was observed to
215 local progression stage (**Fig. 2D**). For example, the "*Harbst melanoma highgrade*" and

216 "*Joensson_Melanoma Pigmentation subtype*" signatures were enriched in RGP and VGP relative to
217 normal, precursor and MIS stages, whereas the opposite was true for "*Harbst melanoma lowgrade*" and
218 "*Joensson_Melanoma Normal like subtype*". Thus, local progression in primary melanoma specimens
219 was associated with the emergence of dedifferentiated states that are similar to states previously
220 characterized in metastatic disease.
221
222 Despite the correspondence between the average disease stage and the average protein or gene
223 expression, CyCIF revealed a high level of specimen-to-specimen difference in the proportions of cells
224 positive for tumor state markers such as MART1, NGFR, SOX9, PRAME and S100A1 or KI67^{+} at each
225 stage (**Fig. 2C**, **Supplementary Fig. S3D,E**). For example, the average proportion of proliferative tumor
226 cells (a feature predictive of poor prognosis[61,62]) increased significantly with stage, but a subset of
227 invasive VGP HRs were as nonproliferative in the tumor compartment (2% Ki67^{+}) as the average
228 precursor field (**Fig. 2C,E**). Similarly, the proportion of MART1^{-} cells in VGP HRs varied from 0% to 100%
229 (**Fig. 2C,H**). MART1 (*MLANA*) levels are controlled by the melanocyte master transcription factor MITF[63]
230 and loss of MART1 expression reflects a fundamental change in tumor differentiation status
231 (**Supplementary Fig. S3F**); MART1 staining is also widely used in melanoma diagnosis.[64] However, we
232 found that it was not the mean proportion of MART1^{-} cells that increased significantly with progression
233 stage but rather the degree of intertumoral variability (as measured by Levene's test; **Fig. 2C**). The
234 proportion of NGFR^{+} tumor cells exhibited a similar trend of increasing variance with stage (e.g., MIS to
235 VGP stages; Levene's test p=0.05, **Fig. 2C**). Note that this type of analysis underestimates the extent of
236 cell-to-cell difference since it binarizes marker levels into plus and minus states and ignores evidence of
237 continuous gradation in expression both within whole specimens and within individual domains of a single
238 specimen (e.g. of MART1; **Fig. 2F-H, Supplementary Fig. S3G, S5H**).

239 **Gene expression programs associated with intra and inter-tumor heterogeneity**
240 To investigate the origins of inter- and intra-tumor heterogeneity, we analyzed gene expression in 900
241 GeoMx tumor and melanocyte MRs using Principal Component Analysis (PCA). This revealed a
242 remarkably well organized trajectory in PCA space from normal HRs (**Fig. 3A** light blue data points) to
243 invasive RGP and VGP HRs on the right (red data points) with extensive intermixing of patient IDs (**Fig**
244 **3B-C; Supplementary Fig. S4A-E**)[13]. When the PCA landscape was annotated using previously
245 established gene expression signatures (e.g. from **Fig. 2D**), we found that MRs lying to the left of PC1
246 corresponded to normal-like melanoma signatures ("*Joensson_Melanoma Normal")* and those on the
247 right to dedifferentiated signatures ("*Landsberg_dedifferentiation_up*", **Fig. 3D,E; Supplementary Fig.**
248 **S4F; Supplementary Fig. S5A-D, Supplementary Fig. S6A-C**). During embryogenesis, melanoblasts
249 arise from the neural-crest lineage and migrate to the epidermis where they mature into melanocytes.[65] It
250 has been proposed that melanocytes expressing neural crest markers, NGFR in particular, represent
251 melanoma initiating cells or cancer stem cells.[66] In our data embryogenic signatures
252 (*Gopalan_Mesenchymal_Early*)[67] were strongly enriched to the right of PC1, coincident with neural crest

253 signatures (e.g. "*Rambow_Neural Crest Stem Cell*") and TGF-β pathway activation (**Supplementary Fig.**
254 **S4G-J**), all of which have previously been associated with dedifferentiated melanocyte states.[68,69]
255 Separation along PC2 corresponded to the strength of the MITF signature: MITF-intermediate states
256 were observed in normal HRs (green outline, **Fig. 3F,G**, **Supplementary Fig. S4G**), MITF-high ("hyper-
257 pigmented") states in invasive melanoma (red outline), and MITF-low dedifferentiated neural-crest like
258 states in invasive VGP HRs (blue outline). Separation of MRs along PC2 is consistent with MITF
259 functioning as a molecular rheostat: MITF-intermediate states were observed in normal HRs (green
260 outline, **Fig. 3F,G**, **Supplementary Fig. S4G**), MITF-high ("hyper-pigmented") states in invasive
261 melanoma (red outline), and MITF-low dedifferentiated neural-crest like states in invasive VGP HRs (blue
262 outline). Thus, MITF activity and tumor cell dedifferentiation emerged as two key features organizing
263 tumor states. In contrast, neither the solar elastosis score (as evaluated at the level of whole specimens)
264 nor the strength of UV transcriptional signatures (at the level of individual MRs) exhibited systematic
265 variation along PC1 or PC2; thus, UV exposure did not appear to be a primary determinant of local tumor
266 cell state (**Fig. 3I**, **Supplementary Fig. S7A-D**) and this was also true of the interferon-γ (IFNγ) or IFNα
267 response signatures (**Supplementary Fig. S4K**, **L**).
268
269 The enrichment of embryonic/neural crest gene sets to the lower right of the PCA landscape was most
270 evident in three deeply invasive specimens (MEL70, MEL72, and MEL74; solid outline in **Fig. 3F,H**)
271 which also exhibited uniformly high NGFR staining in the tumor compartment. Tumor cells arranged in
272 these specimens had a morphology consistent with "vascular mimicry", a histological feature associated
273 with malignancy (**Fig. 3J**)[70] and expressed the highest levels of *NGFR* and the lowest levels of *MLANA*
274 and *MITF* of all specimens (**Supplementary Fig. S5E-G**). We identified one specimen (MEL82; **Fig. 3H**
275 dashed outline) in which NGFR^{+} cells were intermixed with NGFR^{-} tumor cells that expressed SOX10,
276 MART1, and/or SOX9 (**Fig. 3J, Supplementary Fig. S5H**). However, NGFR^{+} cells (and embryonic gene
277 signatures in MRs) were rare or undetectable in earlier progression stages, showing that, in our cohort,
278 an embryonic (neural crest-like) state is unlikely to be involved in melanoma initiation in most tumors.
279
280 Reconciling systematic variation in MR biology across the entire cohort with the intratumoral
281 heterogeneity described in **Fig. 1 & 2** implies that MRs from a single specimen must differ from each
282 other. We found that this was the case: for many specimens, MRs from that specimen were as different
283 from one another as from MRs from all other tumors (note that this analysis used Set A tumors to
284 minimize the impact of the uniformly NGFR-high tumors in Set B; **Fig. 4A, Supplementary Fig. S8A,B**).
285 For example, for MEL18 (a stage IIA melanoma), some MRs with RGP and VGP regions mapped to the
286 left in PC1 (MEL18_015 and _016) and others to the right (MEL18_026 and _027; **Fig. 4B**). The former
287 MRs corresponded to cells growing along the follicular epithelium and invading beyond the follicular
288 adventitia into the surrounding dermis, whereas the latter MRs were located in the dermal invasive
289 component without hair follicle involvement (**Fig. 4B**). In the case of MEL25 (a stage IA melanoma), MRs
290 corresponding to different invasion depths were spread along PC1 with MRs corresponding to the dermal

291 invasive regions (regions MEL25_59 and _65) distinct from the intraepidermal component with superficial
292 invasion (left regions MEL25_61 and MEL25_62, **Supplementary Fig. S8C,D**). Differences in
293 transcriptional signatures between MEL18 and MEL25 MRs were readily discernable in the
294 corresponding CyCIF images, for example partial loss of MART1 in MRs mapped to the left along PC1
295 and retention of MART1 staining in MRs mapped to the right (**Fig. 4A-C** and **Supplementary Fig. S8C-**
296 **E**). These differences were not simply related to the distance between an MR and the dermal-epidermal
297 junction (DEJ), an important consideration since the cellular composition of the skin changes dramatically
298 from epidermis to dermis (**Supplementary Fig. S4D**).
299
300 These data show that the mesoscale cellular neighborhoods corresponding to MRs (200-600 cells or 2-
301 10% of the disease-affected area of a specimen) represent a biologically significant spatial scale for
302 disease-relevant differences in the tumor compartment of primary melanomas (note that these cell
303 numbers represent a 2D slice; a symmetrical 3D MR might therefore be expected to comprise ~ 5×10^3
304 cells). The fact that MR biology can be well described by changes in expression of MITF-regulated and
305 embryonic gene signatures, both of which were first identified in late-stage melanoma, suggests that key
306 features of metastatic disease emerge early in progression. However, these tumor states are not
307 generally present in a pure form either in a single specimen or within a single histological domain (as
308 defined by progression stage) but instead were intermixed at the level of local neighborhoods. Moreover,
309 the continuity of tumor states in PCA space and evidence of continuous variation in protein expression in
310 CyCIF images also suggests that the transition from a normal to an invasive state involves continuous
311 rather than discrete changes in gene expression.

312 **Progression programs in early-stage melanoma**

313 As a complementary approach to analyzing gene expression across MRs we used machine learning
314 based on self-organizing maps (SOMs); this approach projects high-dimensional gene expression onto a
315 two-dimensional grid.[47] We concentrated on earlier stage disease (Set A) and modeled the two batches
316 of GeoMx signatures separately since SOMs were more sensitive to batch effects than PCA analysis (n =
317 299 MRs for Set A1 and n = 239 for Set A2); this yielded 900 metagenes (sets of genes with coordinated
318 expression profiles). We mapped the metagenes onto a two-dimensional representation of the SOM (the
319 SOM portrait) based on their expression pattern and decomposed portraits for each local progression
320 stage. This revealed a well-organized progression series: MRs associated with normal and precursor
321 stages projected onto the lower right corner of the portrait, RGP and VGP stages projected onto the
322 upper left corner, and MIS stages exhibited intermediate projection (**Fig. 5A** and **Supplementary Fig.**
323 **S9A,B**). Thus, the SOM had learned the progression axis from the original data in a fully unsupervised
324 manner, again demonstrating that inter- and intra-tumoral heterogeneity were not random but were
325 associated with an underlying spatial organization.
326

327 To identify transcriptional features contributing to the SOM portrait, metagenes were clustered based on
328 a min-max scaled threshold of 0.95, corresponding approximately to the top 5% of expression value in
329 each metagene profile; this yielded 17 clusters of co-expressed metagenes. These clusters represent key
330 discriminating features in the data and as expected, mapped primarily to the edges of the SOM portrait
331 (Clusters A-Q; **Fig. 5B,C**; **Supplementary Fig. S9C,D**). Cluster N, which existed in the lower right region
332 of the portrait associated with normal and precursor MRs, was enriched in gene expression signatures
333 such as "*Joensson_Melanoma_normal like subtype"* (see **Fig. 2** and **3**). Cluster D in the upper left of the
334 portrait, the location of RGP and VGP MRs, was enriched in signatures of MITF upregulation (e.g.,
335 "*Tirosh_MITF_program*, **Fig. 5C***).* Moreover, when the clusters were projected back to the PC landscape,
336 enrichment scores for clusters N and D corresponded well to the progression trajectory along PC1
337 (**Supplementary Fig. S9E**). The other diagonal of the SOM portrait (dotted line in **Fig. 5B**) was
338 organized by differences in immune and inflammatory signatures, with IFNγ and IFNα signatures in the
339 upper right (cluster P) and other immune features in the lower left (cluster H; **Fig. 5B,C**; see
340 **Supplementary Fig. S9F** for data on all clusters). Dedifferentiation signatures were not a major
341 organizing principle it this particular SOM organization (e.g. *Landsberg_dedifferentiation_up*), probably
342 because dataset A1 was enriched in earlier stage specimens with fewer $NGFR^+$ tumors (the portion of the
343 PCA plot depicted in **Supplementary Fig. S4A,C**).
344
345 To identify the information learned by the SOM we calculated the pairwise correlation among metagenes
346 (Pearson's correlation coefficient, **Supplementary Fig. S9G, Supplementary Fig. S10A**) and then
347 generated a correlation spanning tree (CST, **Fig. 5D, Supplementary Fig. S10B**). A CST represents a
348 cluster map as a partitioned tree, a representation that is easy to parse but does not reduce the fidelity of
349 clustering.[71] We interpreted the resulting CST as having a root and three branches, with the root
350 comprising primarily normal and precursor regions (**Fig. 5D** microregions in blue and green), branch 2
351 comprising MIS regions, and branches 1 and 3 comprising VGP and RGP. Comparing the invasive
352 branches, we found that branch 1 was enriched in MRs from tumors with Breslow depth >1 mm (**Fig. 5E**)
353 and corresponded to clusters D and P of the SOM portrait (**Supplementary Fig. S10C**). MRs in branch 1
354 had higher spatial entropy (**Fig. 5F** and **Supplementary Fig. S10D**) and greater immune-association
355 than MRs from the thinner and more melanocytic (MITF-high) MRs in branch 3 (**Fig. 5G**). Enrichment
356 analysis confirmed that branch 1 was significantly enriched in IFNγ, IFNα, and TNFα responses, and in
357 epithelial-mesenchymal transition (EMT signatures, **Fig. 5H**). To confirm this finding, we compared E-
358 cadherin staining in branch 1 and 3 MRs. E-cadherin is a cell adhesion protein and tumor suppressor,
359 whose loss is a hallmark of EMT commonly observed when melanocytes lose their physical and
360 regulatory links to keratinocytes.[72] We observed a significantly higher proportion of E-cadherin negative
361 cells in branch 1 than branch 3 MRs (**Fig. 5I,J**); overall, E-cadherin intensity levels were positively
362 correlated with MART1 levels (**Supplementary Fig. S10E**). Thus, inflammatory and EMT signatures that
363 were not well resolved by PCA analysis were revealed by the SOM to comprise two (and possibly more)
364 distinct trajectories.

365

366 When MRs making up the CST were labeled by specimen identity, most specimens were found to
367 contain MRs that mapped to multiple branches (**Supplementary Fig. S10F**), consistent with the high
368 intratumoral heterogeneity observed visually and by PCA analysis (**Fig. 3**). For example, stage IB
369 specimen MEL27 formed 6 groups based on their position in the CST (labelled I to VI; **Fig. 5K,**
370 **Supplementary Fig. S10G**). MRs in group I were enriched in MART1$^-$ NGFR$^+$ tumor cells (and a brisk
371 CD8+ T cell infiltrate was present), while group II MRs contained MART1$^+$ NGFR$^-$ cells (**Fig. 5L-N**). MRs
372 in groups II, IV and VI represented the superficial or intraepidermal component of invasive melanoma
373 (**Fig. 5K**). In contrast, MEL14 was an example of a tumor in which all tumor MRs clustered closely
374 together in Branch 1 (**Supplementary Fig. S11A**). These MRs were also similar to each other with
375 respect to tumor cell states, with 92% of tumor cells being MART1$^+$ PMEL$^+$ (**Supplementary Fig.**
376 **S11B,C**). Unsupervised analysis therefore confirms our previous conclusion that MRs from a single tumor
377 can be as variable as MRs from the entire cohort but that high intra-tumoral heterogeneity is not an
378 obligatory feature of primary melanoma.

379 **Spatial features of tumor microenvironment (TME) in melanoma dedifferentiation**

380 To identify spatial features distinguishing CST branches 1 and 3, we used K-means clustering (k = 25) to
381 generate recurrent spatial cellular neighborhoods (RCNs), which separate intermixed cell types into
382 recurrent communities based on local proximity and relative enrichment (**Fig. 6A,B**). The RCNs were
383 then clustered into groups (RCNGs; n = 11) that corresponded to (i) components of the skin such as
384 epidermis, stroma, or vasculature, (ii) immune domains of different types, (iii) tumor domains, and the (iv)
385 tumor-stromal interface (**Fig. 6B-D**). The abundance of epidermis RCNGs (RCNG4) decreased by 10-fold
386 from precursor to VGP while T cell and tumor RCNGs (RCNGs 5 and 1) increased by ~5 - and 25-fold,
387 respectively. In contrast, RCNGs for myeloid/macrophage (RCNG7) and vascular (RCNG11) varied less
388 than 3-fold (**Fig. 6E**). However, the proportions of RCNG7 and RCNG11 were significantly more
389 abundant in the MRs in branch 1 than 3 (**Fig. 6F,G**, **Supplementary Fig. S12A,B**). RCNG7
390 corresponded to a myeloid-rich compartment located either near the invasive front or instead within the
391 dermis as patches alternating with T cells in neighborhood RCNG5. RCNG11 corresponded to blood
392 vessels, visible in **Fig. 6D** in both longitudinal and transverse aspects. To control the possibility that
393 depth-dependent differences in skin composition might confound this analysis, we tested for differences
394 in RCN prevalence with Breslow depth; however, no significant associations were observed
395 (**Supplementary Fig. S12C**). Enrichment of branch 1 MRs for proximity to RCNG11 (myeloid cells) but
396 not RCNG5 (T cells) implies that T cells and myeloid cells were not highly intermixed in most specimens
397 and could therefore differentially pattern the TME. Consistent with this observation, proximity analysis
398 showed that CD8$^+$ T cells were on average the nearest neighbor immune cell type for other CD8$^+$ T cells
399 and macrophages were the closest neighbors to other macrophages (**Supplementary Fig. S12D**).
400 Moreover, branch 1 MRs were found (by CyCIF) to contain a higher proportion of CD163$^+$ and/or CD206$^+$
401 macrophages and CD31$^+$ endothelial cells than branch 3 MRs (**Supplementary Fig. S13A**). We

402 conclude that proximity to myeloid cells was one factor distinguishing branch 1 & 3 cells and that
403 proximity to a vascular/perivasculature environment, an established negative prognostic feature in
404 primary melanoma[73], is another. Thus, it appears that mesoscale architectural features such as blood
405 vessels and clustering of immune cells (myeloid cells in particular) represent substantial contributors to
406 intratumoral heterogeneity.

407 **Quantifying tumor cell state heterogeneity within an MR using spatial entropy**

408 When CyCIF images from individual MRs were examined closely using high dimensional CyCIF it was
409 apparent that tumor cells were not as homogeneous as we had initially postulated when designing the
410 GeoMX sampling strategy (**Fig. 2B, 3J, 4B**). For example, both superficial and deep MRs from MEL18
411 and MEL25 contained neighboring tumor cells expressing SOX9, SOX10 and MART1 in different
412 combinations and intensities, consistent with frequent changes in molecular programs controlling these
413 melanocyte markers (**Fig. 4B,C, Supplementary Fig. S8D,E**). We quantified intermixing using local
414 Shannon entropy, with neighbors defined by Delaunay triangulation on tumor cells (ignoring stromal or
415 immune cells), and cell states as defined in **Fig. 2A**. A low entropy score corresponded to a region of
416 tissue in which tumor cells were similar in type, while a high entropy score corresponded to a spatially
417 intermixed state. Using this approach, we found that some specimens (e.g., MEL18) exhibited low overall
418 entropy whereas others (e.g., MEL25) exhibited high entropy (**Fig. 7A**). However, any single specimen
419 could have both high and low local entropy domains, as evidenced by variability in entropy maps at both
420 the whole-specimen and local levels (**Fig. 7A,B**).
421
422 To identify factors associated with variation in entropy within MRs, we examined MR gene expression
423 profiles and local histology (the spatial entropy used for calculation of MR entropy differed subtly from the
424 single cell entropy described above; see Methods; **Fig. 8A,B**). We observed that, on average, spatial
425 entropy increased significantly with histological stage (e.g., from MIS to RGP or MIS to VGP). NGFR^{+}
426 locally advanced specimens with Breslow depth >4mm in set B were an outlier in this analysis and had
427 the lowest entropy of all specimens in the cohort (**Supplementary Fig. S14D-F**); whether this represents
428 a general evolution of tumor state to greater homogeneity or is a feature of a minority of specimens is not
429 yet known. When mean entropy values for all HRs in a specimen were compared to Breslow depth for
430 that tumor, we found that the average spatial entropy value was constant from thinner to thicker
431 specimens, but the variance increased significantly (as measured by Levene's test; **Fig. 8B**). Since
432 Breslow depth is a specimen-level measurement, we also divided specimens into bands perpendicular to
433 the direction of invasion. In this case, we did not observe a consistent or significant association between
434 local depth of invasion and spatial entropy (**Supplementary Fig. S14A-C**): in many specimens the spatial
435 entropy value was constant with depth, whereas in others it decreased (e.g., MEL18) or increased with
436 depth (MEL58; **Supplementary Fig. S14B**). Thus, it was not the position of cells within a single tumor, as
437 approximated by depth of invasion, that determined the degree of entropy, but rather the overall
438 thickness of the specimen (the Breslow depth), which is a measure of progression. These data

439 demonstrate that the degree of intermixing of tumor cell lineages (the spatial entropy) increases from MIS
440 to VGP stages and the variability in the entropy value also increases as specimens get thicker overall
441 (**Fig. 8B**). These data show that seemingly random fluctuation in state at the length scale of single cells is
442 overlaid in some specimens on changes in mean gene expression at the level of MRs.
443
444 Host immune response has previously been shown to promote lineage plasticity in advanced melanoma[26]
445 and it has been suggested that IFNγ is a primary driver of this plasticity.[74] We therefore asked whether
446 spatial entropy at the level of MRs was associated with proximity to an inflammatory environment. First,
447 we used CyCIF to determine the immune cell composition of MRs having high (n=20) and low (n=20)
448 spatial entropy in the tumor compartment. We found that high entropy regions contained significantly
449 higher proportions of $CD8^+$ T cells and $CD4^+$ $FOXP3^+$ regulatory T cells than low entropy regions (**Fig.**
450 **8C**, **Supplementary Fig. S14G**) and were qualitatively more immune infiltrated, as judged visually using
451 criteria similar to how brisk TIL infiltrates are scored clinically[75] (**Fig. 8D**, **Supplementary Fig. S14H**).
452 Tumor cells in high entropy MRs were also significantly more likely to have nuclear IRF1 (interferon
453 regulatory transcription factor 1), suggesting that they were exposed to IFNγ (**Fig. 8E,F**). Based on gene
454 set enrichment (ssGSEA), high entropy MRs were associated with inflammatory signatures, such as
455 responses to IFNα and IFNγ, classic inflammatory cytokines, the complement pathway, a component of
456 innate immunity, and coagulation (note that the coagulation and complement pathways also contain
457 cytokines and chemokines or their receptors;[76] **Fig. 8G,H**). As an alternative approach we examined the
458 local environment of tumor cells that had lost MART1 expression, which is a univariate measure of tumor
459 cell dedifferentiation and among the most variable of all tumor markers. Using proximity analysis to
460 compare cells within a 15 μm radius of either $SOX10^+$ $MART1^-$ or $SOX10^+$ $MART1^+$ tumor cells, we
461 observed a significant association between loss of MART1 expression and $CD8^+$ T cells, $CD4^+$ Treg cells,
462 macrophages, and endothelial cells (**Supplementary Fig. S13B,C**). We conclude that high entropy in the
463 tumor compartment, and its correlate, tumor cell plasticity, as well as loss of MART1, and its correlate,
464 tumor cell differentiation, are both significantly associated with proximity to immune cells and
465 responsiveness to inflammatory cytokines.
466
467 However, at the level of individual MRs, spatial entropy and local immune reaction were not obligatorily
468 linked: some MRs with high spatial entropy did not exhibit upregulation of inflammatory gene signatures
469 and were not proximate to immune cell populations; the converse was also true (**Fig. 8G,H).** This lack of
470 one-to-one association was also evident in maps of Shannon entropy at single cell resolution: some
471 regions with abundant T cells in close proximity to tumor cells were homogenous and exhibited low
472 Shannon entropy values at single-cell level (**Fig. 7A,B**). Thus, while inflammation can cause spatial
473 entropy, other (unmeasured factors) must be additional contributors.
474
475

476 **DISCUSSION**

477 The high inter- and intra-tumoral heterogeneity observed in primary cutaneous melanoma makes it
478 challenging to study molecular mechanisms promoting tumor initiation, progression, and invasion and
479 greatly complicates diagnosis and risk stratification. Understanding the origins of this heterogeneity, and
480 determining what it means clinically, is likely to be important in improving the treatment of melanoma,
481 particularly when the disease is still curable by surgery (or in high-risk cases, in combination with
482 neoadjuvant therapy)[77] while minimizing overdiagnosis.[6] In this paper, we establish that inter- and intra-
483 tumoral heterogeneity in primary melanomas is not random, but is instead organized with respect to two
484 fundamental axes that specify melanocyte fate: the activity of the MITF transcriptional regulator and
485 expression of neural crest genes associated with a dedifferentiated phenotype. The strength of MITF
486 signatures and the expression of MITF target genes such as *MLANA* (MART1) are intermediate in normal
487 skin and precursor regions, elevated in many RGP and VGP domains (which also over-expressed
488 pigmentation genes), and lowest in invasive VGP domains. This finding is consistent with the rheostat
489 model of MITF inferred from scRNA-Seq of metastatic tumors and melanoma cell lines.[78] The de-
490 differentiated state has also primarily been characterized in metastatic tumors and involves elevated
491 expression of genes associated with progenitor neural crest cells (and with NGFR protein expression)[29].
492 Across all specimens and histological domains in our dataset, the average trajectory of cell states in this
493 MITF v. neural crest landscape was well correlated with local histopathology, demonstrating the
494 existence of defined progression "pathway". Many of the cell state changes observed along this pathway
495 are described as therapy-induced[79], but we find them to be common in early stage treatment-naïve
496 cancers.
497
498 Melanoma cell states are determined not at the level of whole specimens or histological domains but
499 rather locally at the level of MRs. Within a single tumor these MRs vary substantially relative to the
500 average trajectory; thus late-stage tumors often have features characteristic of earlier progenitors and
501 some early-stage tumors have MRs with expression programs characteristic of deep invasion. High
502 variation in tumor cell state from one local region to the next in a single tumor is consistent with the well-
503 established plasticity of melanoma cells[11,80] and it raises the question: what factors drive plasticity and
504 determine cell state? One possibility is diffusible factors and cell-cell contacts in the local
505 microenvironment. Reconstruction of MR state spaces using SOMs and spatial statistics supports this
506 idea and implicate proximity to immune cells and the resulting induction of inflammatory programs.[12] This
507 is consistent with evidence that plasticity[80] and dedifferentiation[27] can be induced by an inflammatory
508 environment in cell lines. Proximity to perivascular spaces is a second factor implicated in fate
509 specification, and this is consistent with the role of angiotropism as a negative prognostic feature in
510 primary melanoma[73] and metastatic disease.[81] However, our data demonstrate that these are not
511 obligatory relationships; for example, melanoma cells can remain in an early progression stage in the
512 face of proximate immune environments, implying the existence of additional spatial regulators.[82]
513

514 A second non-exclusive possibility is that tumor cell state is subject to frequent stochastic fluctuation
515 resulting in a more or less random distribution of states. This does not appear to be a dominant effect at
516 the length scale of MRs, but within some MRs we observe high levels of cell-to-cell variation in the
517 expression of melanocytic markers (quantified here by spatial entropy). Some MRs exhibit high entropy at
518 these short length scales and others do not – and once again proximity to inflammatory environments is
519 implicated. Tumor cell-intrinsic factors are likely to be involved in this type of patterning, based on
520 evidence that some melanoma tumor clones (or induced states) are simply more plastic than others.[82]
521 Genetic instability and clonal evolution are a third possibility, but their spatial properties remain
522 frustratingly difficult to determine in small primary tumors. Stage II specimens such as MEL82 with clear
523 differences in protein expression from one side of a tumor to another are candidates for functionally
524 polyclonal primary cancers.
525
526 **Emergence of embryonic cell states during invasion**
527 Many models of tumorigenesis postulate that embryonic states resembling self-renewing stem cells arise
528 early in disease[83] and promote the development of a diversity of downstream states in response to
529 pressure from immunosurveillance or therapy.[84] However, we find that the dedifferentiated states readily
530 detectable in the invasive components of later stage melanoma are very rarely present in MIS or stage I
531 melanoma; this is true whether induction of neural crest signatures, NGFR protein expression, or
532 expression of embryonic genes is used as a criterion. Interestingly, the least diverse specimens in our
533 cohort were deeply invasive Stage IIb/IIc melanomas. These occupied the extremum of the PCA state
534 landscape and were uniformly populated by NGFR-high tumor cells with a vascular mimicry phenotype.
535 By multiple criteria, these cells were more dedifferentiated than the cutaneous component of Stage III
536 (locally metastatic) tumors also in the dataset. Clinically, deep primary tumors are strongly associated
537 with worse outcomes, with Stage IIB/C disease (primary > 4mm depth invasion) having worse prognosis
538 than shallower Stage IIIA tumors in which the cancer has metastasized to lymph nodes.[4] One possibility
539 is that deep tumors undergo purifying selection as they progress. Alternatively, uniformly NGFR-high
540 tumors might have been “born bad” and progressed rapidly to deep invasion. Analysis of more specimens
541 stratified by recurrence will be necessary to distinguish these possibilities.
542
543 **Factors patterning the melanoma TME and tumor compartment**
544 A picture emerges from this study of tumors strongly influenced by proximity to spatially patterned
545 features of the stroma such as the immune system, basement membranes, and vasculature.[12] For
546 example, decomposition of tumor states using SOMs reveals systematic differences in tumor states
547 adjacent to myeloid or T cell-enriched stromal neighborhoods with proximity to myeloid RCNs associated
548 with a more aggressive and “mesenchymal” state.[85] Blood vessels are spaced every 100-200 μm in the
549 epidermis, generating micro domains that can be predominantly arteriolar, venular, or devoid of
550 microvasculature.[86] Dedifferentiation and loss of expression of cell adhesion proteins such as E-cadherin
551 in melanoma cells is associated with proximity to the vasculature, consistent with the role of angiotropism

552 and embryonic programs in promoting melanoma invasiveness and metastasis.[81] Additional stromal
553 features we have not yet assessed include proximity to nociceptor neurons, which are known to influence
554 immunosurveillance,[87] and follicles, which may restrict melanoma spread.[88]
555
556 None of the significant associations we detect between the TME and tumor cell state are absolute: for
557 example, tumor cell neighborhoods can be dedifferentiated and plastic without evidence of proximity to
558 immune cells and the converse is also true. This suggests that many regulatory interactions and their
559 directionality remain to be identified. Moreover, there is no reason to believe that we have optimally sized
560 the MRs in this study. Although identified based on local morphology, MRs still contained cells of multiple
561 types. A more sophisticated approach to MR definition, the addition of more features of the normal skin,
562 3D maps of nerves and the vasculature, and more refined transcriptional profiling promise to reveal
563 additional factors patterning primary melanomas.
564
565 **Diagnostic implications**
566 Better prognostication of primary melanoma is urgently needed to discriminate low-risk tumors that do not
567 require aggressive treatment or frequent surveillance from those requiring systemic therapy and close
568 monitoring.[89] Use of molecular test for prognostication remains however controversial[90], and American
569 Association of Dermatology guidelines do not recommend molecular testing (outside of clinical trials) due
570 to insufficient evidence of efficacy.[91] The current study raises four questions impinging on this
571 controversy and prognostication more generally. First, does progression of a tumor along the MITF v.
572 neural crest landscape correspond to risk of metastasis or recurrence and if so, how might these states
573 best be measured in clinical specimens? Second, does a tumor that is largely at an early progression
574 state but has some MRs with late-stage properties represent a high-risk tumor? Third, is high intratumoral
575 variation (high cell state entropy) itself a risk feature? Fourth, to what extent are any of these properties
576 correlated with or explanatory of established diagnostic features such as Breslow depth? It is noteworthy
577 that prognostic tests currently being developed or marketed rely primarily on bulk gene expression
578 profiling (e.g. CP-GEP[92], Skyline DX®[93], DecisionDX®[94] etc.) that inevitably obscures intratumoral
579 heterogeneity. If a risk feature is recessive (e.g., a reduction in gene expression in an MR) then it may be
580 very difficult to reliably detect using bulk assays. Thus, spatial approaches that build on current
581 dermatopathology practice such as multiplexed imaging combined with machine learning on H&E
582 images[95] may represent a superior approach.
583
584 **ACKNOWLEDGEMENTS**
585 This work was supported by the Ludwig Center at Harvard an ASPIRE Award from The Mark Foundation
586 for Cancer Research, and NCI grants U2C-CA233262 to PKS, SS; NCI grants R00-CA256497 to AJN
587 and R50-CA252138 to ZM. TV is supported by a Research Scholar Grant, PF-24-1316850-01-CD, from
588 the American Cancer Society. Histopathology support was provided by P30-CA06516. SS is supported

589 by the BWH President's Scholars Award. We thank Kerrie Marie and Vishaka Gopalan for their help and
590 expertise in this project.

591 **Author contributions**
592 **Conceptualization.** TV, YS, ANJ, ZM, YRS, GM, SS, DL, CL and PKS
593 **Formal Analysis.** TV, YS, EN, SP, GW, YRS
594 **Funding acquisition** SS, DL, PKS
595 **Investigation** TV, YS, SP, RP, ZM
596 **Supervision** YRS, GM, SS, DL, CL and PKS
597 **Writing** TV, YS, JBT, PKS
598

599 **DATA AND SOFTWARE AVAILABILITY**
600 GeoMx gene expression data will be available via the Gene Expression Omnibus (GEO;
601 RRID:SCR_005012). All CyCIF images with associated histopathological and GeoMx MR annotations will
602 be available to explore online via Minerva software[96], which supports zoom, pan, and selection actions
603 without requiring the installation of software or downloading the images, at the Harvard Tissue Atlas
604 (https://www.tissue-atlas.org/). **Supplementary Video S1** gives an overview of how to navigate between
605 channel groups and visualize annotations using Minerva. Selected CyCIF channels for specimen MEL14
606 can be explored via Minerva at https://www.cycif.org/data/vallius-
607 2025/early_melanoma_tumor_intrinsic_e41/MEL14-A3/index.html. Full-resolution CyCIF images, single
608 cell segmentation masks, and cell count tables will be available via the NCI Human Tumor Atlas Network
609 data portal (https://data.humantumoratlas.org/); see **Supplementary Table S1** for a mapping of sample
610 numbers to HTAN IDs. Note that individual image files are ∼100 GB in size. Code used for multimodal
611 spatial analysis are available on GitHub (https://github.com/labsyspharm/2025-Vallius-Shi-Novikov-
612 melanoma-PCAII).
613

614 **METHODS**

615 **Clinical samples**
616 FFPE specimens of primary cutaneous melanoma were retrospectively identified from the archives of the
617 Brigham and Women's and Massachusetts General Hospitals (n=62 patients, MEL14 to MEL86; see
618 **Supplementary Table S1** for HTAN identifiers and associated clinical metadata). The samples were
619 collected under Institutional Review Board approval (Primary IRB:2019P003828, Secondary IRB: 21-
620 0656) under a waiver of consent. Two sets of specimens were acquired and deeply annotated: sample
621 set A (n=45) was selected for the presence of multiple disease stages within the same sample with an
622 emphasis on stage I melanoma. Sample set B (n=17) was selected for the presence of later stage II
623 disease; multiple stages were often present in these specimens, but this was not a selection criterion.
624 Fresh FFPE tissue sections were cut from each tumor block. The first section of each block was H&E-
625 stained and used to annotate histopathological ROIs (**Fig. 1C** and **Supplementary Fig. S1B**). The

626 remaining subsequent sections were used for cyclic multiplex immunofluorescence imaging (CyCIF)
627 experiments to characterize markers of melanoma progression and the features of the immune
628 microenvironment within various stages of melanoma. A fresh cut of the samples was performed for
629 deeper profiling with microregion transcriptomic profiling using GeoMx Digital Spatial Profiling (DSP)
630 technology. The clinical, biospecimen, and imaging-level metadata were all collected following the
631 Minimum Information about Highly Multiplexed Tissue Imaging (MITI) standards[97].
632 Based on the melanoma diagnostic criteria, the histopathologic annotations included normal skin (N),
633 Precursor (P), Melanoma *in situ* (MIS), Radial Growth Phase melanoma (RGP), and Vertical Growth
634 Phase melanoma (VGP). These ROIs were further classified and subdivided based on the presence of
635 immune infiltrate (brisk TIL, non-brisk TIL, absent). In the case that a single specimen contained more
636 than one histologic region in each category (e.g., precursor regions on both sides of vertical growth
637 phase melanoma), we performed neighborhood analyses separately, as these regions were not
638 physically adjacent.

639 **Imaging (H&E and tissue-based CyCIF)**

640 H&E-stained FFPE sections from each tissue block were imaged using a CyteFinder slide scanning
641 fluorescence microscope (RareCyte Inc.) with a 20×/0.75 NA objective with no pixel binning. Serial FFPE
642 sections (5 μm thick) were subjected to whole-slide, subcellular resolution, 34 to 49-plex CyCIF imaging
643 with two different antibody panels to generate complementary datasets (**Fig. 1C** and **Supplementary**
644 **Fig. S1B, S2B**). CyCIF panels 1 and 3 were used for general immune phenotyping to fully profile the
645 tumor microenvironment, and panel 2 was used to better understand the tumor intrinsic features.
646 Antibody information and associated RRIDs are listed in **Supplementary Table S1**. CyCIF was
647 performed as described in[98] and more specifically at protocols.io
648 (dx.doi.org/10.17504/protocols.io.j8nlkoqbdv5r/v1). In brief, the BOND RX Automated IHC Stainer was
649 used to bake FFPE slides at 60°C for 30 minutes, dewax using Bond Dewax solution at 72°C, and
650 perform antigen retrieval using Epitope Retrieval 1 (Leica) solution at 100°C for 20 minutes. Slides
651 underwent multiple cycles of antibody incubation, imaging, and fluorophore inactivation. Antibodies were
652 incubated overnight at 4°C in the dark. Before imaging, a 0.15mm single-sided self-adhesive spacer was
653 applied to the slide, followed by wet-mounting of a glass coverslip using 50% glycerol in 1× PBS. This
654 helps to greatly reduce friction during coverslip removal, ultimately preserving the tissue structure
655 between cycles. Images were acquired using the same microscope and objective as the H&E images.
656 Slides were soaked in 42°C PBS to facilitate coverslip removal, and then fluorophores were inactivated
657 by incubating slides in a solution of 4.5% H_2O_2 and 24 mmol/L NaOH in PBS and placing them under an
658 LED light source for 1 hour. Only antibodies that had passed a multi-step validation process and followed
659 the expected staining pattern were included in downstream analysis.

660 **CyCIF image pre-processing and quality control**

661 Stitching individual CyCIF images together into a high-dimensional representation for further
662 segmentation and analyses was done using the open-source MCMICRO pipeline[58] (RRID:SCR_022832),

663 an open-source multiple-choice microscopy pipeline
664 (version:38182748aa0ec021f684ce47248c57340d2f4cc7; full codes available on at
665 https://github.com/labsyspharm/mcmicro). Specific parameters used were optimized after iterative
666 inspection of results, specifically focused on performance of the segmentation module to ensure accurate
667 identification of single cells (params.yml files available at https://github.com/labsyspharm/2025-Vallius-
668 Shi-Novikov-melanoma-PCAII). After generating the segmentation masks, the mean fluorescence
669 intensities of each marker for each cell were computed, resulting in a single-cell data table for each
670 acquired whole-slide CyCIF image. The X/Y coordinates of annotated histologic regions on the whole-
671 slide image were used to extract the single-cell data of cells that lie within the ROI range.
672 Multiple approaches were also taken to ensure the quality of the single-cell data. At the image level, the
673 cross-cycle image registration and tissue integrity were reviewed; regions that were poorly registered or
674 contained severely deformed tissues and artifacts were identified, and cells inside those regions were
675 excluded. Antibodies that gave low confidence staining patterns by visual evaluation were also excluded
676 from the analyses. The quality of the segmentation was assessed, and the segmentation parameters
677 were iteratively modified to improve the accuracy of the segmentation masks.

678 **CyCIF single-cell phenotyping**

679 We used a gating-based phenotyping approach to classify cells as described previously.[12] In short, an
680 open-source visual gating tool (https://github.com/labsyspharm/gater) was used to derive gates for each
681 marker. Similar to batch correction, the identified gates for each marker were then used to rescale the
682 single-cell data between 0 and 1, such that the values above 0.5 identify cells that express the marker
683 and vice versa. The scaled single-cell data was then used for cell-type calling. Tools within the SCIMAP[99]
684 python package (RRID:SCR_024751) were used to then assign phenotype labels to individual cells
685 based on a hierarchical classification of staining patterns (**Supplementary Fig. S2C**, **Fig. 2A,B**,
686 **Supplementary Table S1,4**). The assigned cell types were verified by overlaying the phenotypic labels
687 onto the images.

688 **Correlation between protein markers and RNA levels**

689 We performed correlation analysis between expression levels of melanoma gene expression, tumor state
690 pathway scores, and CyCIF quantification of MRs across samples. The pairwise Spearman correlation
691 coefficients were calculated based on the log-transformed RNA level, protein expression level, and
692 pathway scores, as well as CyCIF quantification of each GeoMx ROIs. Pairwise correlation was
693 calculated between those categories. Positive correlation was represented by red circles, with stronger
694 correlations shown by darker and large circles. In contrast, negative correlations were represented by
695 blue circles, with stronger negative correlations shown by darker and larger circles. Non-significant or
696 weak correlations are smaller circles or absent circles near zero.

Spatial entropy and identification of invasion bands

The local neighborhood Shannon entropy was calculated for each tumor cell according to its nearest neighbors defined via a Delaunay triangulation for the whole-slide images. In order to extend the notion of classical Shannon entropy to spatial entropy, spatial information was incorporated by forming a network graph G = (V, E) using the single cells per tissue specimen. The nodes V of the graph were defined according to the spatial location of single cells and edges E were specified via a Delaunay triangulation. Single-cell neighbors were defined by nearest neighbors in the resulting graph structure and edges were weighted by the Euclidean distance between single cells in tissue space. The graph G was also instantiated as a node attribute graph where each node (single-cell) was assigned the corresponding single cell phenotype (see Methods, CyCIF single-cell phenotyping). Numerous extensions and variations of entropy measures have been proposed in the literature.[100,101] The spatial entropy metric used here extends the intuition of Wang and Zhao[102] in classifying landscapes in ecological studies whereby the Shannon entropy is augmented by a prefactor that is directly proportional to the intermixing strength and inversely proportional to the distance between nearest neighboring single cells of different phenotypes. The intermixing strength for each phenotype is defined as the cumulative total of the number of nearest neighbor single cells with differing phenotypes across all local neighborhoods. Given the scale differences between microscopy and ecological data, a scaling factor α is used here for visualization purposes. The form of spatial entropy employed in this work (is to the authors' knowledge applied for the first time in the single-cell microscopy domain) was chosen for its objective and intuitive nature, as well as prior success in discerning spatial structure between varying ecological landscapes. The mathematical form of the spatial entropy H implemented in the single-cell analysis in this manuscript is detailed below:

$$H = \sum_{l=1}^{L} \frac{\alpha \frac{1}{n_l} \sum_{i=1}^{n_l} M_{i,l}}{\frac{1}{n_l} \sum_{i=1}^{n_l} D_{i,l}} p_l \log_2 p_l ,$$

where the intermixing strength $M_{i,l}$ for cell i with attribute l is defined as,

$$M_{i,l} = \sum_{j=1}^{k_i} \mathbb{I}(c_j \neq l)$$

and the distance $D_{i,l}$ for cell i with attribute l is defined as,

$$D_{i,l} = \sum_{j=1}^{k_i} d_{ij} \, \mathbb{I}(c_j \neq l) .$$

The variables and notation is defined as follows, L is the number of attributes, e.g., single-cell tumor phenotypes, n_l is the number of single cells with attribute l in the tissue, k_i is the number of nearest neighbors of cell i, c_j is the attribute of cell j, d_{ij} is the distance between cell i and cell j, $\mathbb{I}$ is the indicator

725 function which equals 1 if the condition is satisfied and 0 otherwise, α is a scaling factor described above,
726 and p_l is the probability of attribute l in the tissue.
727
728 An open-source software package SpatialCells[103] was used to identify subregions with a thickness of
729 0.2mm based on distance from the epidermis (invasion bands, **Supplementary Fig. S14A**). An
730 increment of 0.2mm was used to separate each subregion. Local progression stages were further split
731 into disjoint spatial subsections (in order not to bias the spatial analysis) and the spatial entropy H was
732 calculated in each subregion.

733 **Recurrent cellular neighborhood (RCN) analysis**

734 CyCIF neighborhood analyses were performed using the functions *spatial_count* and *spatial_cluster*
735 within the SCIMAP[99] python package. For each single cell in the CyCIF data, we determined the local
736 neighborhood composition by querying a radius of 50 pixels (15 microns) from the cell centroid as
737 measured by the Euclidean distance between X/Y coordinates. The cell types of these cellular neighbors
738 and their frequencies were identified to generate a neighborhood matrix containing the neighbor
739 phenotype information for every single cell in the data (*spatial_count*). The neighborhood matrix was then
740 clustered using k-means clustering with *k* = 25 (*spatial_cluster*). The optimal number of *K*-means
741 clustering was determined by looking for the elbow point in the computed cluster heterogeneity during
742 convergence (**Supplementary Fig. S13D**). The clusters were then grouped into RCNGs (n=11) based on
743 similarity of the microenvironmental composition. The RCNG assignments were visually confirmed by
744 overlaying the RNCGs on multiple CyCIF images.

745 **Microregion transcriptomics (GeoMx®) processing, data collection and annotation**

746 For GeoMx digital spatial profiling (DSP), we used NanoString GeoMx human whole transcriptome atlas
747 (WTA) RNA probes to profile the histopathological annotated regions mentioned above using previously
748 described methods[50]. Briefly, freshly cut (< 2 weeks) 5 µm thick FFPE sections were baked at 60℃ for 3
749 hours, dewaxed, and hybridized with the WTA probes overnight. On the following day, the slides were
750 incubated with fluorescence-conjugated antibodies targeting melanocytes and tumor cells
751 (SOX10/MLANA), epithelial cells (pan-CK), and immune cells (CD45) before imaging and transcript
752 collection on the DSP (**Supplementary Fig. S1D**, **Supplementary Table S1**). These fluorescent signals
753 were used for ROI selection and for probe collection of 1,266 ROIs representing morphologically distinct
754 sites (N, P, MIS, RGP, VGP; **Fig. 1C**). The collected probes were pooled for library preparation and sent
755 out for Next Generation Sequencing (Biopolymers Facility at Harvard Medical School). In addition to the
756 annotations for local progression axis, the selected GeoMx microregions were annotated for location and
757 immune responses. The annotations for location included epidermis (melanocyte and tumor regions in
758 normal/precursor/MIS and the superficial intra-epidermal component above the RGP and VGP regions),
759 tumor center, stroma, margin (invasive tumor front), and periphery (regions at the periphery of VGP either
760 separate of the main tumor mass, or presenting with discohesive tumor cells at the periphery of VGP
761 without a solid invasive front), tumor center, other). Immune responses for the microregions were

762 annotated by visually assessing the CD45 staining and the cell morphology and were classified as brisk,
763 non-brisk, or absent for RGP and VGP regions, and as immune response or no immune for N, P, and
764 MIS regions.

765 **GeoMx trajectory analysis**

766 Principal components analysis (PCA) was performed on the tumor (tumor/melanocytic annotated) MRs
767 from all datasets (Sets A1, A2, B1, B2, e.g., **Fig. 3A-I**) without batch correction. Tumor MRs were
768 projected onto the first two principal components (PC), with PC1 and PC2 explaining 28% and 14% of the
769 variance, respectively. The inferred developmental trajectory, depicted as a black line, was computed
770 using the *Slingshot* package (https://github.com/kstreet13/slingshot; RRID:SCR_017012) based on PC1
771 and PC2 embeddings. In addition, a separate trajectory analysis was performed on Set1 tumor MRs
772 using PCA following batch correction with the *limma* package (e.g., **Fig. 4A**; RRID:SCR_010943).

773 **Differential gene expression and pathway analysis**

774 Differential gene expression analysis was performed using the *DESeq2* package[104] (RRID:SCR_015687).
775 The top 60 differentially expressed genes (DEGs) were used for pathway enrichment analysis using the
776 *fgsea* package (https://github.com/alserglab/fgsea) (e.g., in **Fig. 5H**). Additionally, normalized and $\log_{10}$-
777 transformed expression matrices extracted from *DESeq2* were used to compute single-sample Gene Set
778 Enrichment Analysis (ssGSEA) scores using the *GSVA* R package
779 (https://www.bioconductor.org/packages/release/bioc/vignettes/GSVA/inst/doc/GSVA.html,
780 RRID:SCR_021058; e.g., **Fig. 8G**).

781 **Self-organizing map (SOM) and the correlation spanning tree**

782 Gene expression data from GeoMx Set A1 and Set A2 were log10-transformed, quantile normalized and
783 centralized on a gene-wise basis by subtracting the mean log expression of each gene (averaged across
784 all samples) from its observed value. The processed data were then clustered using a self-organizing
785 maps (SOMs) machine learning method[105], resulting in 900 co-expressed metagenes (SOM was
786 conducted within Set A1 and Set A2 separately due to batch effect issue). The so-called SOM-portrayal
787 method was used to visualize the general gene expression levels of metagenes using a two-dimensional
788 quadratic 30 x 30 pixel map and a maroon-to-blue color code for high-to-low metagene expression
789 values.[105,106] Local progression stage -specific mean portraits were generated by averaging the metagene
790 landscapes of all cases belonging to one category and difference portraits between them were calculated
791 as the difference between the metagene values in each grid of these maps. Clusters of co-expressed
792 metagenes were identified by selected so-called “cluster areas” in the SOM portraits using
793 overexpression criteria as described previously.[105] The metagene Clusters (**Fig. 5B** and **Supplementary**
794 **Fig. S9C,F**) were determined in unsupervised fashion as previously described.[105]
795
796 A pairwise correlation analysis (Pearson’s correlation coefficient) was calculated using the metagene
797 expression profiles among all tumor ROIs. The correlation matrix was then used to construct a correlation

spanning tree, where each node represents a ROI and the edges represent the correlation strength between the ROIs. Based on the location of the nodes in the correlation spanning tree, each ROI was assigned a Branch ID (Branch 1, 2, or 3).

Statistical Tests

All statistical tests to infer *P* value for significant differences between groups were performed using the Mann-Whitney U rank test with either *mannwhitneyu* function in the *scipy* Python package (RRID:SCR_008058) or *stats* and *ggpubr* R packages. The difference in the spatial entropy score variance within Breslow depth categories was tested with the Levene's test using *car* R package.

Figure 1.

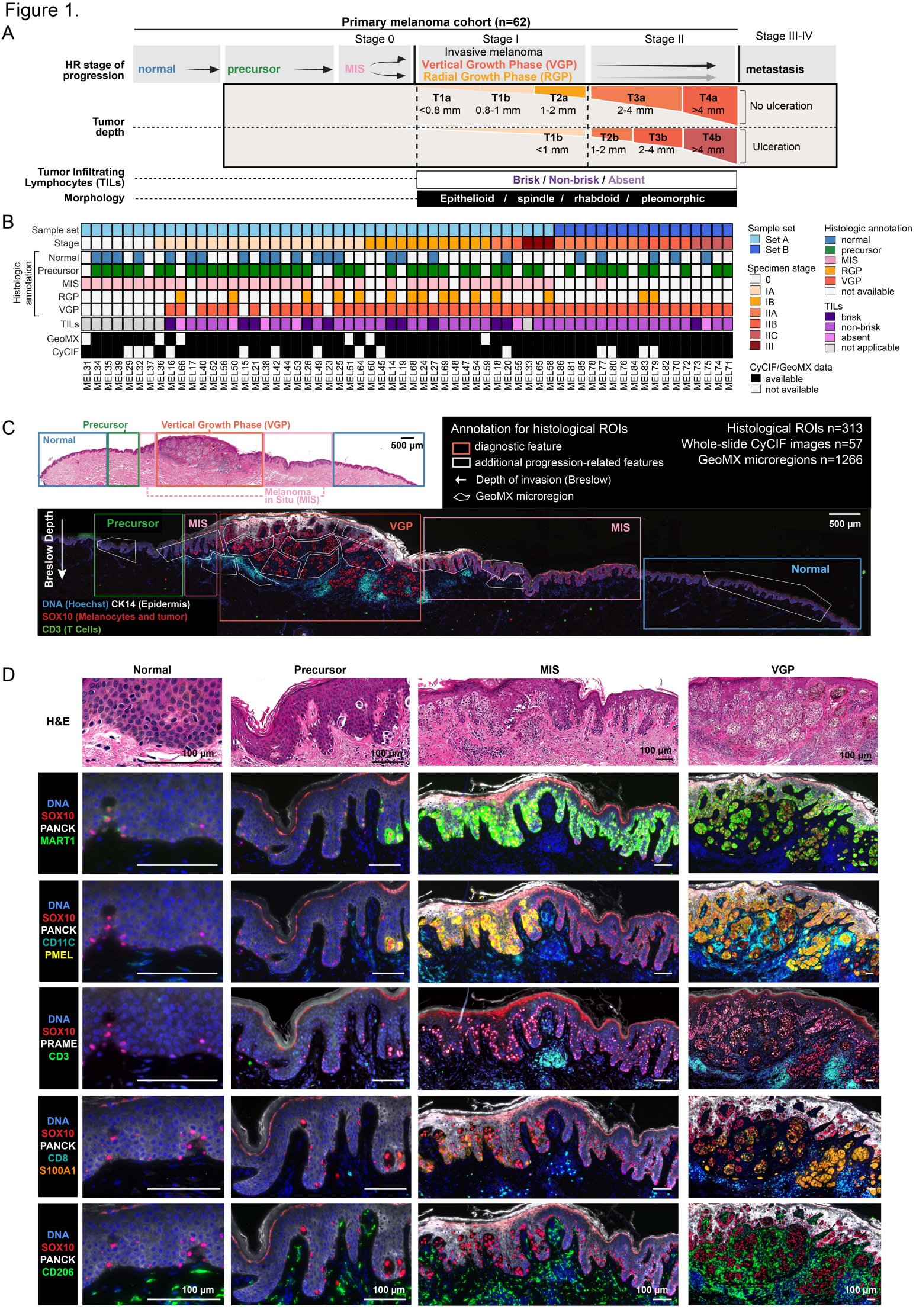
A
Primary melanoma cohort (n=62)
Stage 0
Stage I
Stage II
Stage III-IV
HR stage of progression
normal
precursor
MIS
Invasive melanoma
Vertical Growth Phase (VGP)
Radial Growth Phase (RGP)
metastasis
Tumor depth
T1a <0.8 mm
T1b 0.8-1 mm
T2a 1-2 mm
T3a 2-4 mm
T4a >4 mm
No ulceration
T1b <1 mm
T2b 1-2 mm
T3b 2-4 mm
T4b >4 mm
Ulceration
Tumor Infiltrating Lymphocytes (TILs)
Brisk / Non-brisk / Absent
Morphology
Epithelioid / spindle / rhabdoid / pleomorphic
B
Sample set
Stage
Histologic annotation
Normal
Precursor
MIS
RGP
VGP
TILs
GeoMX
CyCIF
Sample set
Set A
Set B
Specimen stage
0
IA
IB
IIA
IIB
IIC
III
Histologic annotation
normal
precursor
MIS
RGP
VGP
not available
TILs
brisk
non-brisk
absent
not applicable
CyCIF/GeoMX data
available
not available
C
Precursor
Vertical Growth Phase (VGP)
Normal
500 µm
Melanoma in Situ (MIS)
Annotation for histological ROIs
diagnostic feature
additional progression-related features
Depth of invasion (Breslow)
GeoMX microregion
Histological ROIs n=313
Whole-slide CyCIF images n=57
GeoMX microregions n=1266
Breslow Depth
Precursor
MIS
VGP
MIS
Normal
500 µm
DNA (Hoechst) CK14 (Epidermis)
SOX10 (Melanocytes and tumor)
CD3 (T Cells)
D
Normal
Precursor
MIS
VGP
H&E
100 µm
DNA SOX10 PANCK MART1
DNA SOX10 PANCK CD11C PMEL
DNA SOX10 PRAME CD3
DNA SOX10 PANCK CD8 S100A1
DNA SOX10 PANCK CD206

807 **Figure 1. Multimodal profiling of primary melanoma.**

808 **A.** Summary of the current AJCC 8th edition for cutaneous melanoma staging[41] based on features
809 identified from H&Es. **B.** Overview of the primary melanoma cohort used for multimodal spatial profiling
810 and their associated clinical (AJCC) and histological characteristics. (TILs: Tumor-infiltrating lymphocytes;
811 normal skin; precursor; MIS: melanoma in situ; RGP: radial growth phase melanoma; VGP: vertical
812 growth phase melanoma). **C.** Example specimen (MEL14) annotated with clinical histological stages
813 (colored rectangles), as H&E (top) and CyCIF image of a serial section (bottom). CyCIF image shows a
814 subset of markers: DNA (blue), CK14 (epidermis; white), SOX10 (melanocytes and tumor cells; red), and
815 CD3 (T cells; green). White polygons overlaid represent the microregions (MRs) used for spatial
816 transcriptomics (GeoMx). Arrow indicates the measurement and direction of Breslow depth. Scale bars,
817 500 μm. **D.** Examples of histopathological features annotated in the specimen MEL14. Top row: Fields of
818 view of a H&E-stained section with four major histologic regions indicated: adjacent normal melanocytes
819 and skin, melanocytic atypia (precursor), melanoma in situ (MIS), vertical growth phase melanoma.
820 Bottom rows: Corresponding CyCIF images showing staining for a variety of tumor and immune markers.
821 See **Supplementary Table S3** for how markers related to cell types. Scale bars, 100 μm.

Figure 2.

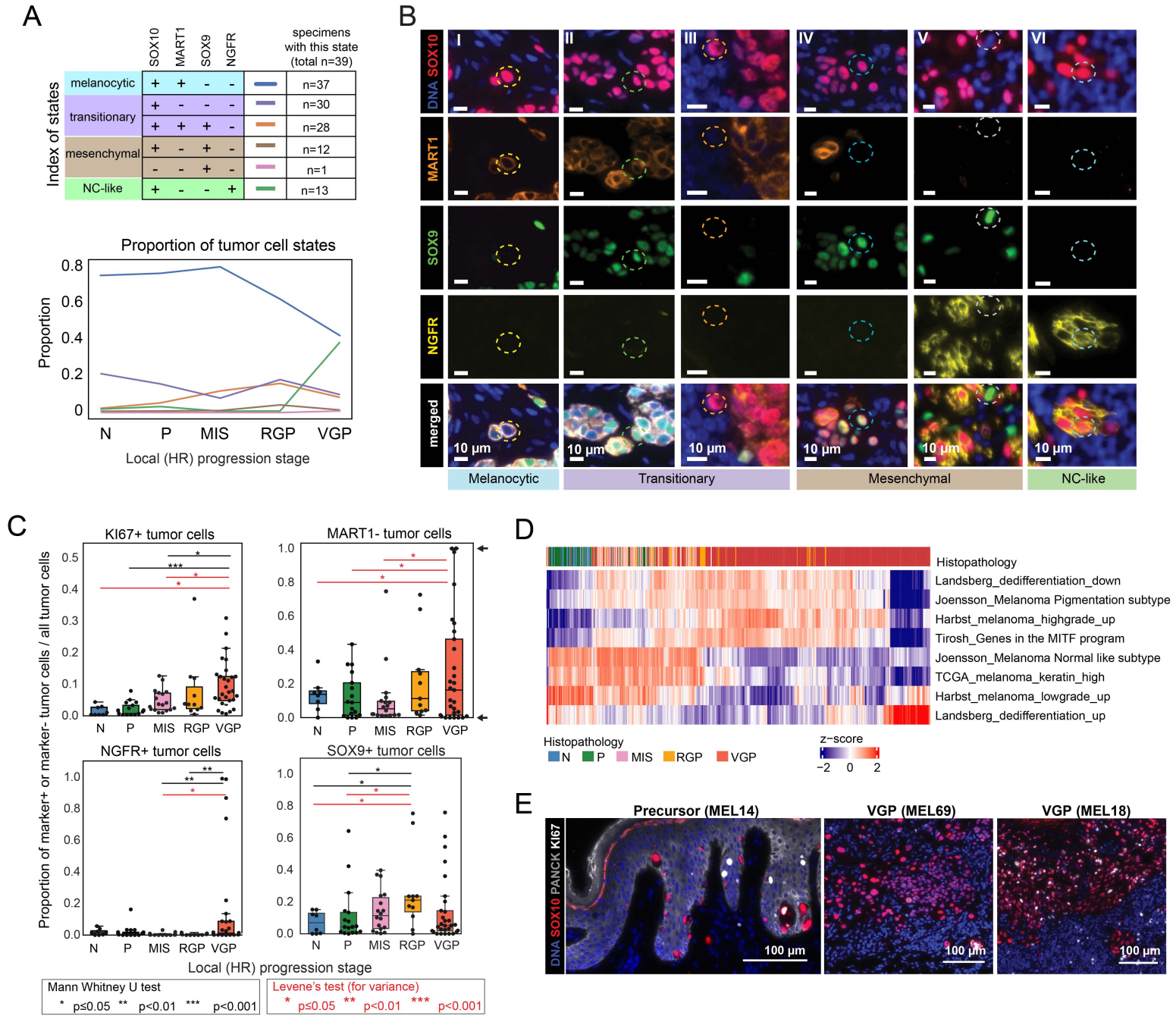
A
SOX10
MART1
SOX9
NGFR
specimens with this state (total n=39)
Index of states
melanocytic
transitionary
mesenchymal
NC-like
n=37
n=30
n=28
n=12
n=1
n=13
Proportion of tumor cell states
Proportion
Local (HR) progression stage
N
P
MIS
RGP
VGP
B
DNA SOX10
MART1
SOX9
NGFR
merged
10 µm
Melanocytic
Transitionary
Mesenchymal
NC-like
C
KI67+ tumor cells
MART1- tumor cells
NGFR+ tumor cells
SOX9+ tumor cells
Proportion of marker+ or marker- tumor cells / all tumor cells
Local (HR) progression stage
Mann Whitney U test
* p≤0.05 ** p<0.01 *** p<0.001
Levene's test (for variance)
* p≤0.05 ** p<0.01 *** p<0.001
D
Histopathology
Landsberg_dedifferentiation_down
Joensson_Melanoma Pigmentation subtype
Harbst_melanoma_highgrade_up
Tirosh_Genes in the MITF program
Joensson_Melanoma Normal like subtype
TCGA_melanoma_keratin_high
Harbst_melanoma_lowgrade_up
Landsberg_dedifferentiation_up
z-score
E
Precursor (MEL14)
VGP (MEL69)
VGP (MEL18)
DNA SOX10 PANCK KI67
100 µm
F
DNA SOX10 NGFR MART1 panCK
MEL14
Breslow 1.1mm
Stage IB
Panel G
500 µm
20 µm
MEL71
Breslow 7mm, Stage IIB
MEL74
Breslow 5.4mm, Stage IIB
G
DNA SOX10 MART1
50 µm
H
MEL14
MEL71
MEL74
MART1 levels
Proportion of tumor cells
MART1-
MART1+
500 µm

823 **Figure 2. Association of melanocytic differentiation with progression and intertumoral**
824 **heterogeneity**

825 **A.** Tumor cell states annotated according to the binarized staining of protein markers for SOX10, MART1,
826 SOX9 and NGFR (upper panel). The mean proportion of each melanocyte and tumor cell state within
827 local stages of progression (N, P, MIS, RGP and VGP; lower panel). **B**. CyCIF images showing
828 examples of single cells representing the protein-based tumor cell states detected in the primary
829 melanoma cohort samples. The magnified regions labeled as I-VI from **Supplementary Fig. S3B**,
830 stained for DNA (blue), SOX10 (red), MART1 (orange), SOX9 (green) and NGFR (yellow). Scale bars, 10
831 µm. **C.** The proportion of SOX10+ melanocytes or tumor cells expressing KI67, MART1, NGFR and
832 SOX9 grouped by histologic regions (HR). Each data point represents a sample proportion, calculated
833 from a single sample. MannWhitney U test (black) and Levene's test (red) *, $P < 0.05$; **, $P < 0.01$; ***, P
834 < 0.001. Box represents the first and third interquartiles of the data, whiskers extend to show the rest of
835 the distribution except for points that are determined to be outliers. See **Supplementary Table S5** for the
836 CyCIF quantification. **D.** Heatmap showing mean expression (z-scored) of melanoma associated
837 signatures within melanocyte and tumor GeoMx MRs annotated for local stages of progression. **E**. CyCIF
838 images of specimen MEL14, MEL69 and MEL18, showing selected fields of view stained for DNA (blue),
839 SOX10 (red), KI67 (white), PanCK (gray). **F**. CyCIF images of specimens MEL14 (left), MEL71 (middle)
840 and MEL74 (right), showing a subset of markers: DNA (blue), epidermis (panCK: white), and
841 melanocyte/tumor (SOX10: red, NGFR: yellow, MART1: green). Colored rectangles represent magnified
842 regions at right. Scale bars, 500 µm and 20 µm. **G.** Selected fields of view of CyCIF images from panel F
843 (white rectangles), showing DNA (blue), SOX10 (red), and MART1 (green). Scale bars, 50 µm. **H.** Scatter
844 plots showing mean MART1 fluorescence intensity for tumor cell and melanocyte cell centroids for
845 invasive regions from MEL14, MEL71 and MEL74. The centroids for other cell types (non-tumor cells) are
846 shown with grey dots. The proportion of $MART1^{+}$ and $MART1^{-}$ tumor cells (binarized call with gate 0.5) is
847 shown on the right of each scatter plot. Scale bars, 200 µm.

Figure 3.

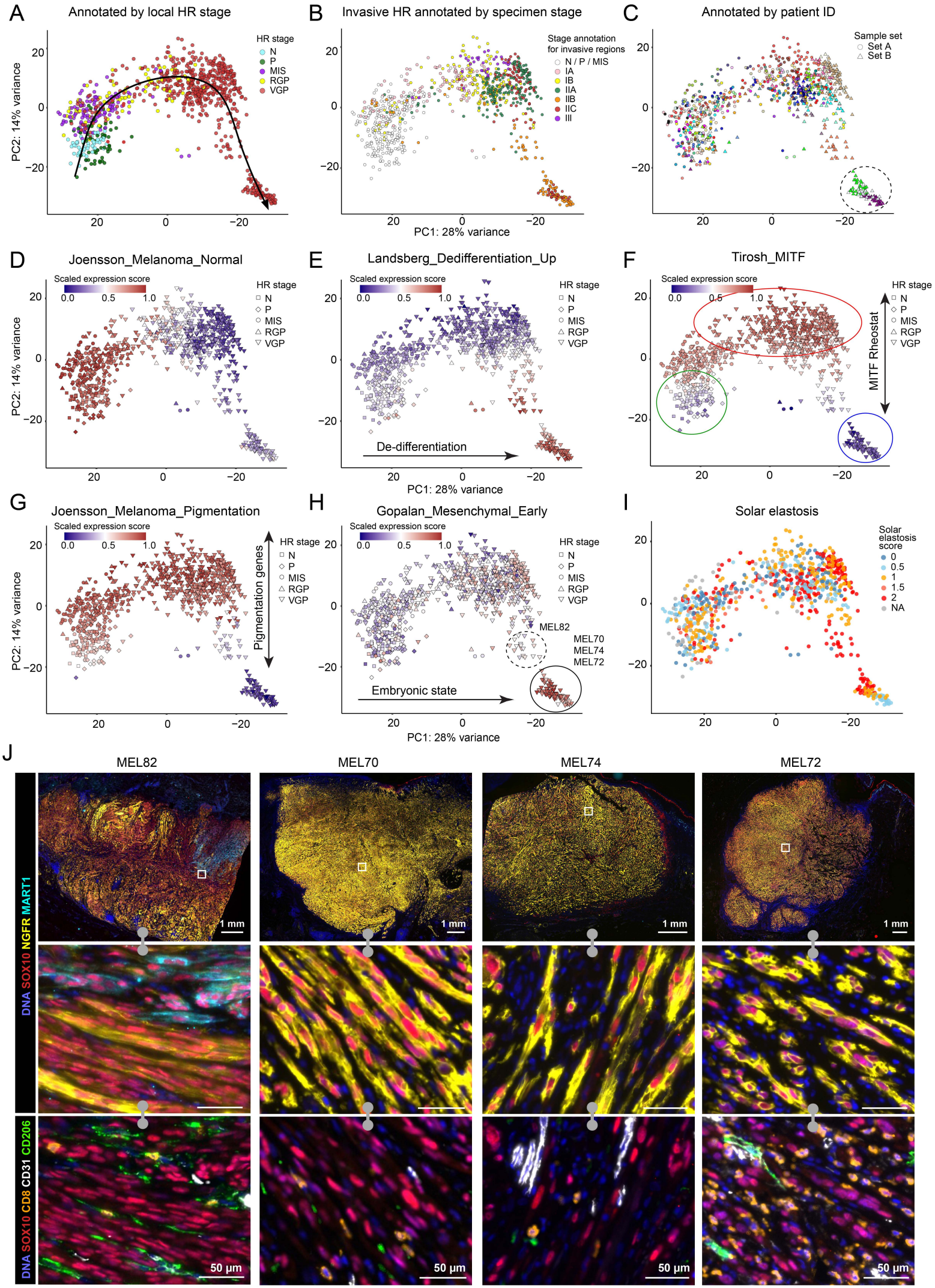
A
Annotated by local HR stage
HR stage
N
P
MIS
RGP
VGP
PC2: 14% variance
B
Invasive HR annotated by specimen stage
Stage annotation for invasive regions
N / P / MIS
IA
IB
IIA
IIB
IIC
III
PC1: 28% variance
C
Annotated by patient ID
Sample set
Set A
Set B
D
Joensson_Melanoma_Normal
Scaled expression score
E
Landsberg_Dedifferentiation_Up
De-differentiation
F
Tirosh_MITF
MITF Rheostat
G
Joensson_Melanoma_Pigmentation
Pigmentation genes
H
Gopalan_Mesenchymal_Early
MEL82
MEL70
MEL74
MEL72
Embryonic state
I
Solar elastosis
Solar elastosis score
0
0.5
1
1.5
2
NA
J
MEL82
MEL70
MEL74
MEL72
DNA SOX10 NGFR MART1
DNA SOX10 CD8 CD31 CD206
1 mm
50 µm

849 **Figure 3. Intra- and inter-tumoral transcriptomic heterogeneity in primary melanoma.**

850 **A-C.** Principal component (PC) analysis plots of GeoMx spatial transcriptomic data from microregions
851 (MRs) representing melanocytes and tumor cells, with colors indicating histopathological annotations (**A**),
852 specimen stage, AJCC 8th edition (**B**), and patient ID and sample set (**C**). Annotations are shown in
853 **Supplementary Fig. S4A** and **S4B**. Each data point represents a single GeoMx MR. **D-H**. PC analysis
854 plots of GeoMx spatial transcriptomic data from MRs representing melanocytes and tumor cells, colored
855 by the enrichment scores for previously published melanoma-related and Hallmark gene signatures:
856 *Joensson_Melanoma_Normal* (**D**)*, Landsberg_dedifferentiation_up* (**E**)*, Tirosh_MITF* (**F**)*,*
857 *Joensson_Melanoma_Pigmentation* (**G**)*, Gopalan_Mesenchymal_Early* (**H**)*.* **I**. PC analysis plots of
858 GeoMx spatial transcriptomic data from melanocytes and tumor cells, colored by the solar elastosis score
859 (specimen-level annotation)*.* **J.** CyCIF images of specimens MEL82, MEL70, MEL74, and MEL72 stained
860 with a subset of tumor, immune, and stromal markers: DNA (blue), and melanocyte/tumor (SOX10: red,
861 NGFR: yellow, MART1: cyan), CD8^{+} T cells (CD8: orange), endothelial cells (CD31: white), CD206^{+}
862 macrophages (CD206: green). Top row shows low magnification view, with rectangles corresponding to
863 the ROIs magnified in the middle and bottom rows. Scale bars, 1 mm and 50 μm.

Figure 4.

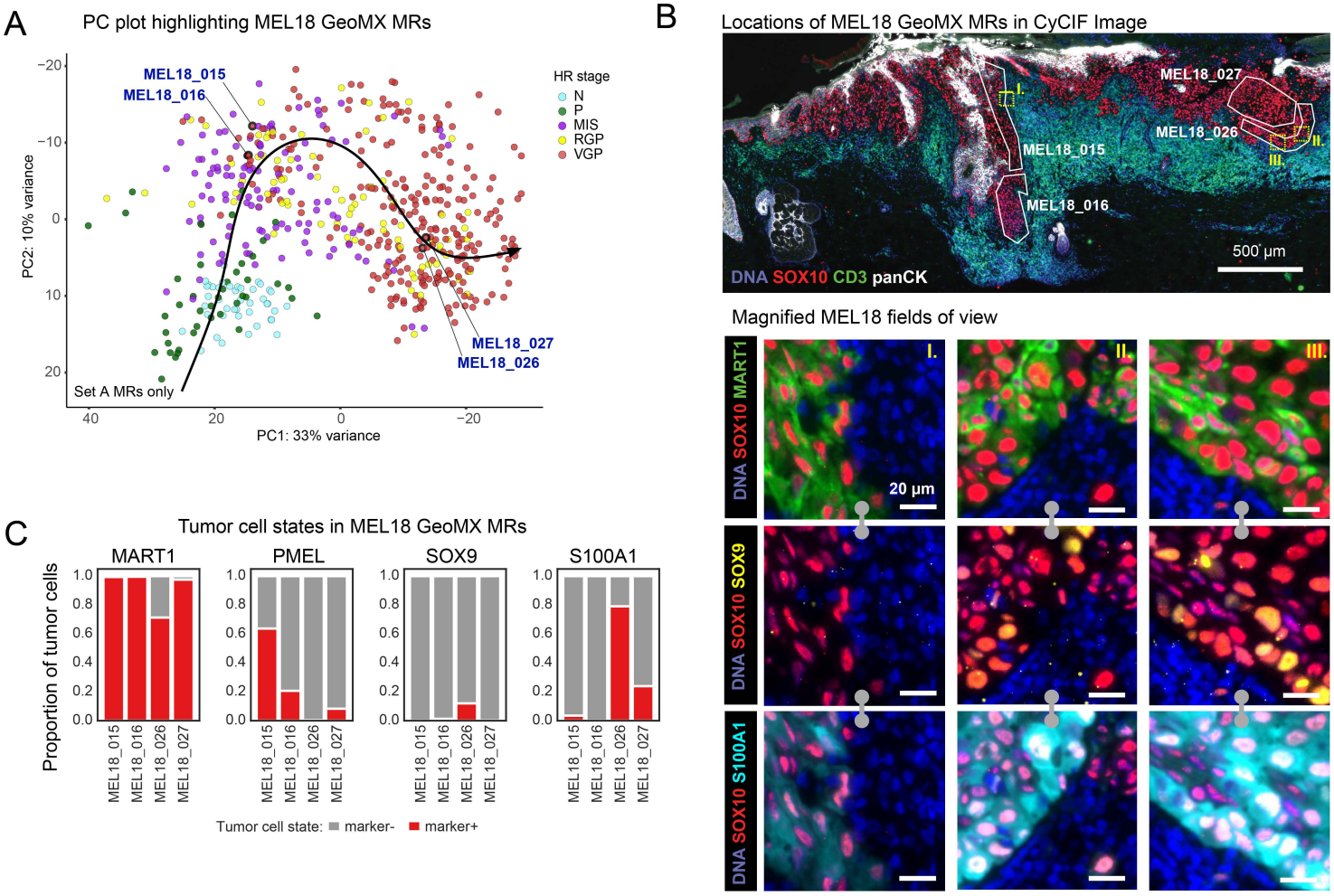
A
PC plot highlighting MEL18 GeoMX MRs
MEL18_015
MEL18_016
MEL18_027
MEL18_026
Set A MRs only
HR stage
N
P
MIS
RGP
VGP
PC2: 10% variance
PC1: 33% variance
B
Locations of MEL18 GeoMX MRs in CyCIF Image
MEL18_027
MEL18_026
MEL18_015
MEL18_016
I.
II.
III.
500 µm
DNA SOX10 CD3 panCK
Magnified MEL18 fields of view
DNA SOX10 MART1
DNA SOX10 SOX9
DNA SOX10 S100A1
20 µm
C
Tumor cell states in MEL18 GeoMX MRs
MART1
PMEL
SOX9
S100A1
Proportion of tumor cells
MEL18_015
MEL18_016
MEL18_026
MEL18_027
Tumor cell state: marker- marker+

865 **Figure 4. Tumor state heterogeneity within GeoMx MRs.**

866 **A.** PC plot of all GeoMx spatial transcriptomic data from microregions (MRs) representing melanocytes
867 and tumor cells in sample Set A, colored by histological annotations. Each data point represents a single
868 GeoMx MR. Four exemplary MRs from specimen MEL18 are highlighted (MRs MEL18_015, MEL18_016,
869 MEL18_027, MEL18_026). **B.** Top: CyCIF image of MEL18 labeled with the spatial locations of selected
870 VGP GeoMx microregions (white polygons). MRs are labeled with MR ID, indicating how the regions
871 correspond to the PC plot in panel C. Lower: Magnified ROIs from top panel showing various tumor cell
872 state markers, including SOX10 (red), MART1 (green), SOX9 (yellow). Scale bars, 500 μm and 20 μm.
873 **C.** The proportion of tumor cells positive for MART1, PMEL, SOX9 and S100A1 within selected VGP
874 GeoMx microregions from specimen MEL18.

Figure 5.

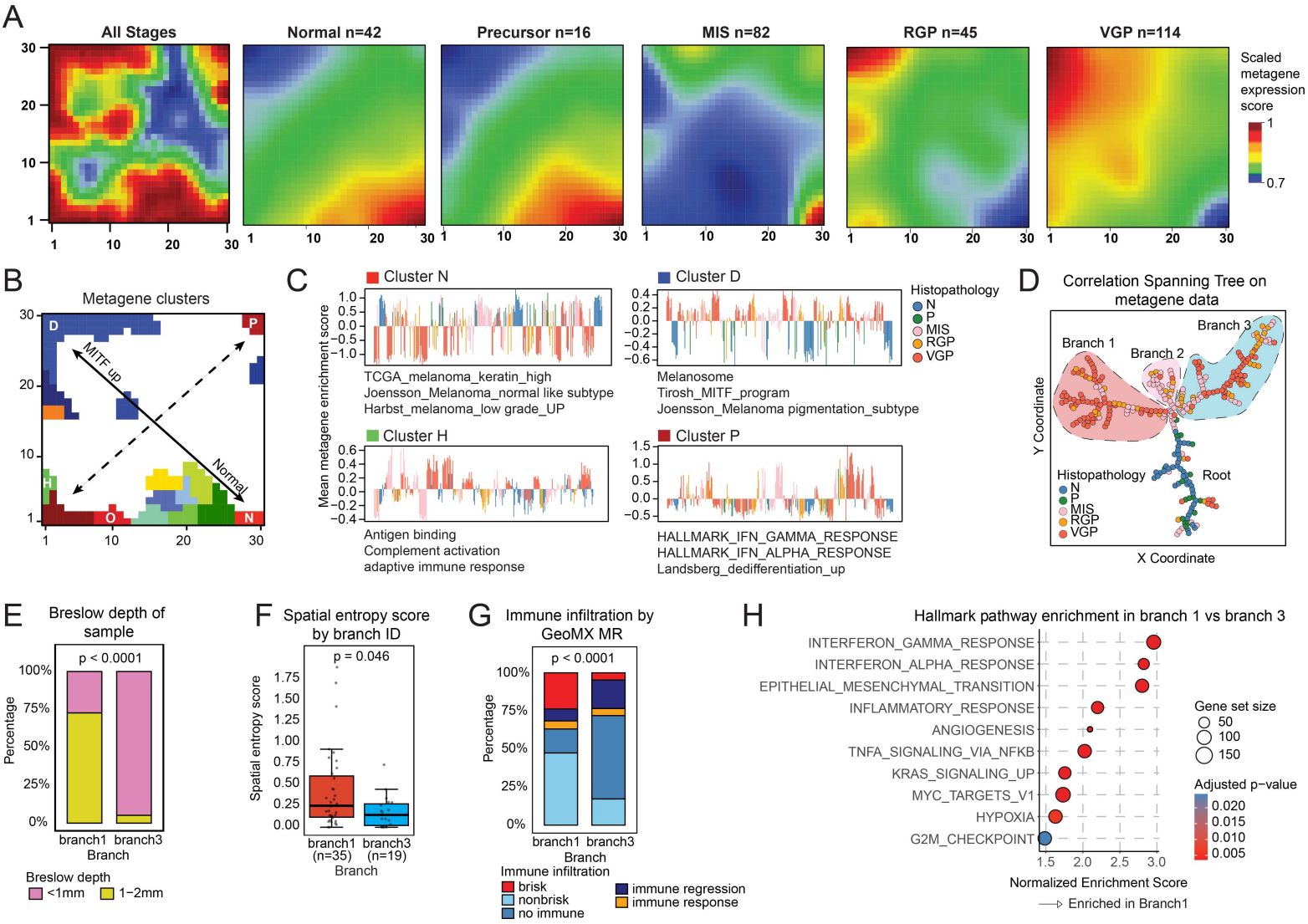
A
All Stages
Normal n=42
Precursor n=16
MIS n=82
RGP n=45
VGP n=114
Scaled metagene expression score
B
Metagene clusters
MITF up
Normal
C
Cluster N
Cluster D
Cluster H
Cluster P
Mean metagene enrichment score
Histopathology
N
P
MIS
RGP
VGP
TCGA_melanoma_keratin_high
Joensson_Melanoma_normal like subtype
Harbst_melanoma_low grade_UP
Melanosome
Tirosh_MITF_program
Joensson_Melanoma pigmentation_subtype
Antigen binding
Complement activation
adaptive immune response
HALLMARK_IFN_GAMMA_RESPONSE
HALLMARK_IFN_ALPHA_RESPONSE
Landsberg_dedifferentiation_up
D
Correlation Spanning Tree on metagene data
Branch 1
Branch 2
Branch 3
Root
Y Coordinate
X Coordinate
E
Breslow depth of sample
p < 0.0001
Percentage
branch1
branch3
Branch
Breslow depth
<1mm
1−2mm
F
Spatial entropy score by branch ID
p = 0.046
Spatial entropy score
branch1 (n=35)
branch3 (n=19)
G
Immune infiltration by GeoMX MR
p < 0.0001
Immune infiltration
brisk
nonbrisk
no immune
immune regression
immune response
H
Hallmark pathway enrichment in branch 1 vs branch 3
INTERFERON_GAMMA_RESPONSE
INTERFERON_ALPHA_RESPONSE
EPITHELIAL_MESENCHYMAL_TRANSITION
INFLAMMATORY_RESPONSE
ANGIOGENESIS
TNFA_SIGNALING_VIA_NFKB
KRAS_SIGNALING_UP
MYC_TARGETS_V1
HYPOXIA
G2M_CHECKPOINT
Gene set size
Adjusted p−value
Normalized Enrichment Score
Enriched in Branch1
I
Loss of E-cadherin expression
p=0.05
proportion of tumor cells
branch 1
branch 3
J
DNA SOX10 MART1 ECAD
500 µm
50 µm
K
MEL27 MR Groups I to VI
Y Coordinate
X Coordinate
MEL27
Other
DNA SOX10 CD3 panCK
GeoMX region
L
Composition of MEL27 CST Groups
Group I
Group II
Group IV
Group V
Group VI
GeoMX MR ID
Tumor state
MART1- NGFR- SOX9-
MART1+ NGFR- SOX9-
MART1- NGFR- SOX9+
MART1+ NGFR- SOX9+
MART1- NGFR+ SOX9-
M
DNA PANCK SOX10 MART1
DNA PANCK SOX10 NGFR
MEL27
500 µm
N
DNA SOX10 CD8 panCK
DNA SOX10 CD8 CD11C
MEL27
500 µm
50 µm

876 **Figure 5. Developmental trajectory from normal melanocytes to invasive melanoma.**
877 **A.** Self-organizing map (SOM) portrait of GeoMx data (Set A1, n = 299 from n = 28 patients), showing the
878 global expression of 900 metagenes across profiled samples (left). Each square within the 30x30 grid
879 represents an unique metagene. SOM portraits for local progression stages show the global expression
880 of 900 metagenes in microregions (MRs) grouped by histopathology. The expression levels of each
881 metagene are indicated with a color (scaled metagene expression score) as compared to the average
882 expression of all metagenes. **B.** SOM clusters A-Q and their mapping to the SOM portrait. Unique SOM
883 clusters are indicated with unique colors. Spots N, D, H, P and O are highlighted, and the rest are shown
884 in **Supplementary Fig. S9F**. **C.** Mean expression profiles of the defined SOM clusters N, D, H and P
885 within microregions from various progression stage categories. The Y axis represents the mean
886 expression profile of the SOM cluster signatures of each microregion. Individual MRs are shown in the X
887 axis. The pathways listed below represent the most enriched pathways within each SOM cluster. **D.**
888 Minimum spanning tree analysis showing the correlation of profiled GeoMx MRs. The datapoints (colored
889 circles) represent individual MRs. The correlation spanning tree (CST) is annotated by the local
890 progression stage for each MR and the branch identity (Branches 1, 2 and 3). **E.** The percentage of MRs
891 in Branches 1 and 3 belonging to samples with Breslow depth <1mm and 1-2 mm. P-value was
892 calculated based on Fisher's exact test. **F.** Spatial entropy scores calculated for the corresponding tumor
893 regions in the adjacent tissue section for Branch 1 and 3 MRs. Each data point represents a spatial
894 entropy score calculated for individual GeoMx MRs, and the samples are grouped by the CST branch
895 identity. P-value was calculated based on Wilcoxon Rank Sum test. **G.** The proportion of annotations for
896 immune responses (brisk TIL, non-brisk TIL, no immune, immune regression, immune response) within
897 Branch 1 and 3 MRs. P-value was calculated based on Fisher's exact test. **H.** Gene-set enrichment
898 analysis (GSEA) of Hallmark gene set (pathways) significantly enriched in Branch 1 and Branch 3
899 microregions. Dot size indicates the size of the gene set and color indicates the adjusted *p* value. **I.** The
900 proportion of tumor cells staining positive for E-cadherin of all tumor cells in Branch 1 and Branch 3
901 microregions. Each data point represents the mean proportion of marker+ cells within a single GeoMx
902 MR, and the samples are grouped by the CST branch identity. **J.** CyCIF image of specimen MEL54
903 stained for DNA (blue), SOX10 (cyan), MART1 (red), E-cadherin (yellow), highlighting two GeoMx
904 microregions from Branch 1. Scale bars, 500 μm and 50 μm. **K.** Left: CST highlighting microregions from
905 specimen MEL27 (yellow dots). The grey datapoints represent individual MRs from other patients. Groups
906 of microregions are encircled with different colors and annotated with roman numerals (I-VI). A subset of
907 these microregions is highlighted in the CyCIF images on the right. **L.** The proportion of various tumor cell
908 states within selected VGP GeoMx microregions from specimen MEL27. Cluster ID indicates the grouping
909 of MRs shown in the correlation spanning tree in panel K. **M.** CyCIF image of specimen MEL27 stained
910 for DNA (blue), SOX10 (red), panCK (white), MART1 (green; top row), and NGFR (yellow; bottom row).
911 **N.** Top: CyCIF image of specimen MEL27 stained for DNA (blue), SOX10 (red), panCK (white) and CD8
912 (green). Bottom: magnified regions indicated with I and II are stained for DNA (blue), SOX10 (red), CD8
913 (green) and CD11C (yellow).

Figure 6.

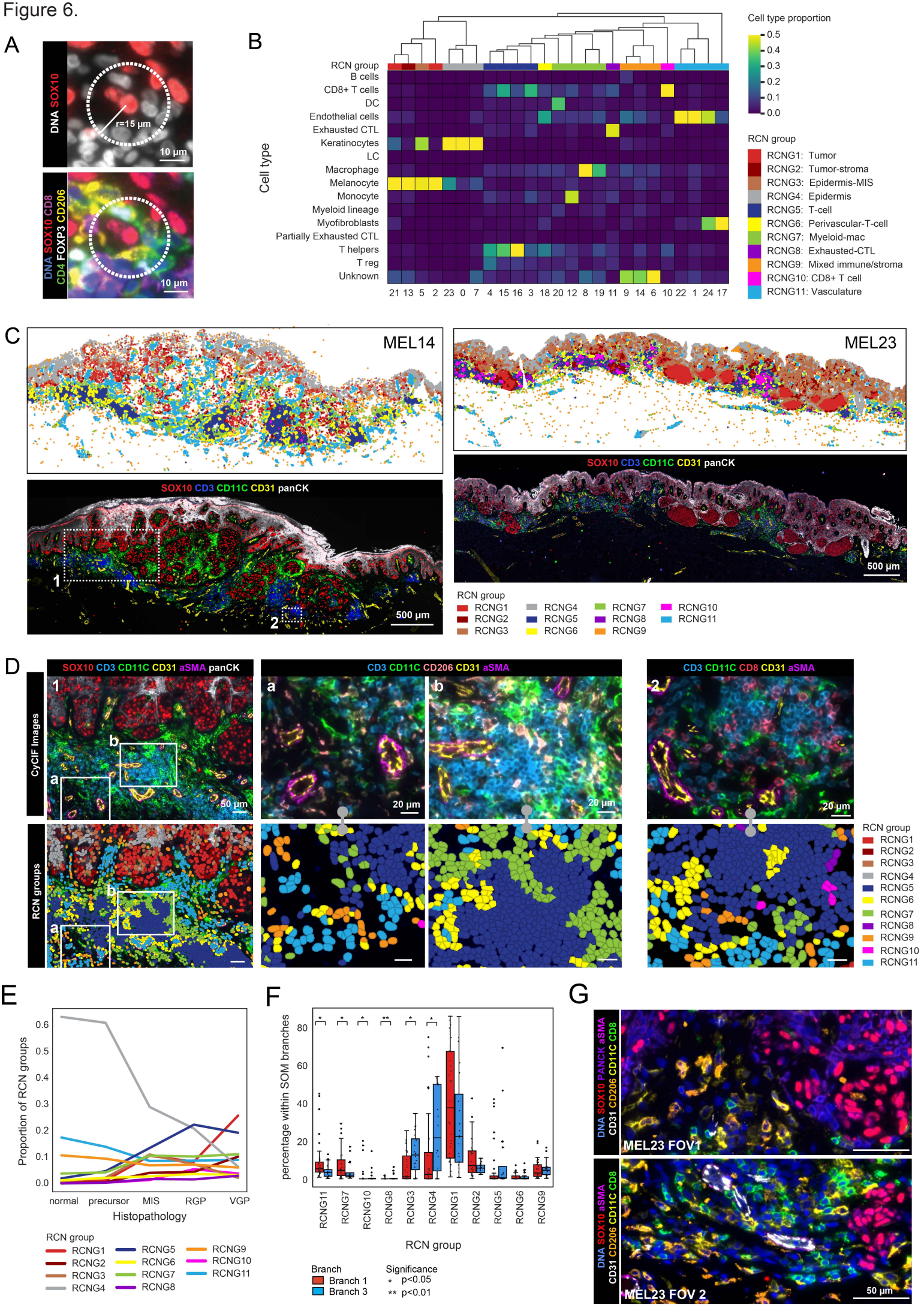
A
DNA SOX10
r=15 µm
10 µm
DNA SOX10 CD8
CD4 FOXP3 CD206
10 µm
B
Cell type proportion
0.5
0.4
0.3
0.2
0.1
0.0
RCN group
Cell type
B cells
CD8+ T cells
DC
Endothelial cells
Exhausted CTL
Keratinocytes
LC
Macrophage
Melanocyte
Monocyte
Myeloid lineage
Myofibroblasts
Partially Exhausted CTL
T helpers
T reg
Unknown
21 13 5 2 23 0 7 4 15 16 3 18 20 12 8 19 11 9 14 6 10 22 1 24 17
RCNG1: Tumor
RCNG2: Tumor-stroma
RCNG3: Epidermis-MIS
RCNG4: Epidermis
RCNG5: T-cell
RCNG6: Perivascular-T-cell
RCNG7: Myeloid-mac
RCNG8: Exhausted-CTL
RCNG9: Mixed immune/stroma
RCNG10: CD8+ T cell
RCNG11: Vasculature
C
MEL14
MEL23
SOX10 CD3 CD11C CD31 panCK
1
2
500 µm
RCN group
RCNG1
RCNG2
RCNG3
RCNG4
RCNG5
RCNG6
RCNG7
RCNG8
RCNG9
RCNG10
RCNG11
D
SOX10 CD3 CD11C CD31 aSMA panCK
CD3 CD11C CD206 CD31 aSMA
CD3 CD11C CD8 CD31 aSMA
CyCIF Images
RCN groups
50 µm
20 µm
E
Proportion of RCN groups
0.6
0.5
0.4
0.3
0.2
0.1
0.0
normal
precursor
MIS
RGP
VGP
Histopathology
RCN group
F
percentage within SOM branches
80
60
40
20
0
RCNG11
RCNG7
RCNG10
RCNG8
RCNG3
RCNG4
RCNG1
RCNG2
RCNG5
RCNG6
RCNG9
RCN group
Branch
Branch 1
Branch 3
Significance
* p<0.05
** p<0.01
G
DNA SOX10 PANCK aSMA
CD31 CD206 CD11C CD8
MEL23 FOV1
DNA SOX10 aSMA
CD31 CD206 CD11C CD8
MEL23 FOV 2
50 µm

915 **Figure 6. Spatial features of tumor microenvironment (TME) in melanoma dedifferentiation**

916 **A.** CyCIF image of a field of view in specimen MEL18 showing an example of a cellular neighborhood
917 with a 15 μm (50 px) radius, stained for DNA (blue), SOX10 (red; left). The corresponding region (right)
918 stained for DNA (blue), SOX10 (red), CD8 (purple), CD4 (green), FOXP3 (white), CD206 (yellow). Scale
919 bars, 10 μm. **B.** A heatmap showing the mean proportion of cell types within Recurrent Cellular
920 Neighborhoods (k=25) and their grouping into 11 meta clusters (RCN groups: RCNG). **C.** Top: Scatter
921 plots showing the RCN annotations for each cell within selected fields of view for samples MEL14 (left)
922 and MEL23 (right). Each datapoint represents a cell centroid in the corresponding CyCIF image. The
923 corresponding CyCIF image is shown below for both tumors, stained for SOX10 (red), CD3 (blue),
924 CD11C (green), panCK (white), CD31 (yellow). Scale bars, 500 μm. **D.** Magnified regions 1 and 2 from
925 specimen MEL14 shown in panel C. Top left: Region 1 stained for SOX10 (red), CD3 (blue), CD11C
926 (green), panCK (white), CD31 (yellow), aSMA (magenta). Bottom left: Region 1 with RNCG annotations
927 for each single cell. Middle: magnified insets a and b from Region 1 stained for CD3 (blue), CD11C
928 (green), CD206 (orange), CD31 (yellow), aSMA (magenta), and their corresponding RCNG annotations.
929 Top right: Region 2 stained for CD3 (blue), CD11C (green), CD8 (red), CD31 (yellow), and aSMA
930 (magenta). Bottom right: Region 2 with RNCG annotations for each single cell. Scale bars, 50 μm and 20
931 μm. **E.** The proportion of RCN groups (RCNG1-11) within local progression stage HRs (normal,
932 precursor, MIS, RGP, VGP). **F.** RCNG identities of single cells belonging to Branch 1 and Branch 3
933 microregions. Box plots show the proportion of cells within Branch 1 and Branch 3 belonging to different
934 RCNGs in each CyCIF sample. Each datapoint represents the mean percentage of RCNGs within each
935 sample, and the samples are grouped by their correlation spanning tree identity (Branch 1 vs Branch 2).
936 *, $P < 0.05$; **, $P < 0.01$. **G.** Magnified fields of view from specimen MEL23 (CyCIF image shown in
937 **Supplementary Fig. S12B**). Staining for DNA (blue), SOX10 (red), panCK (purple; top panel only),
938 aSMA (magenta), CD31 (white), CD206 (orange), CD11C (yellow), and CD8 (green) are shown. Scale
939 bars 50 μm.

Figure 7.

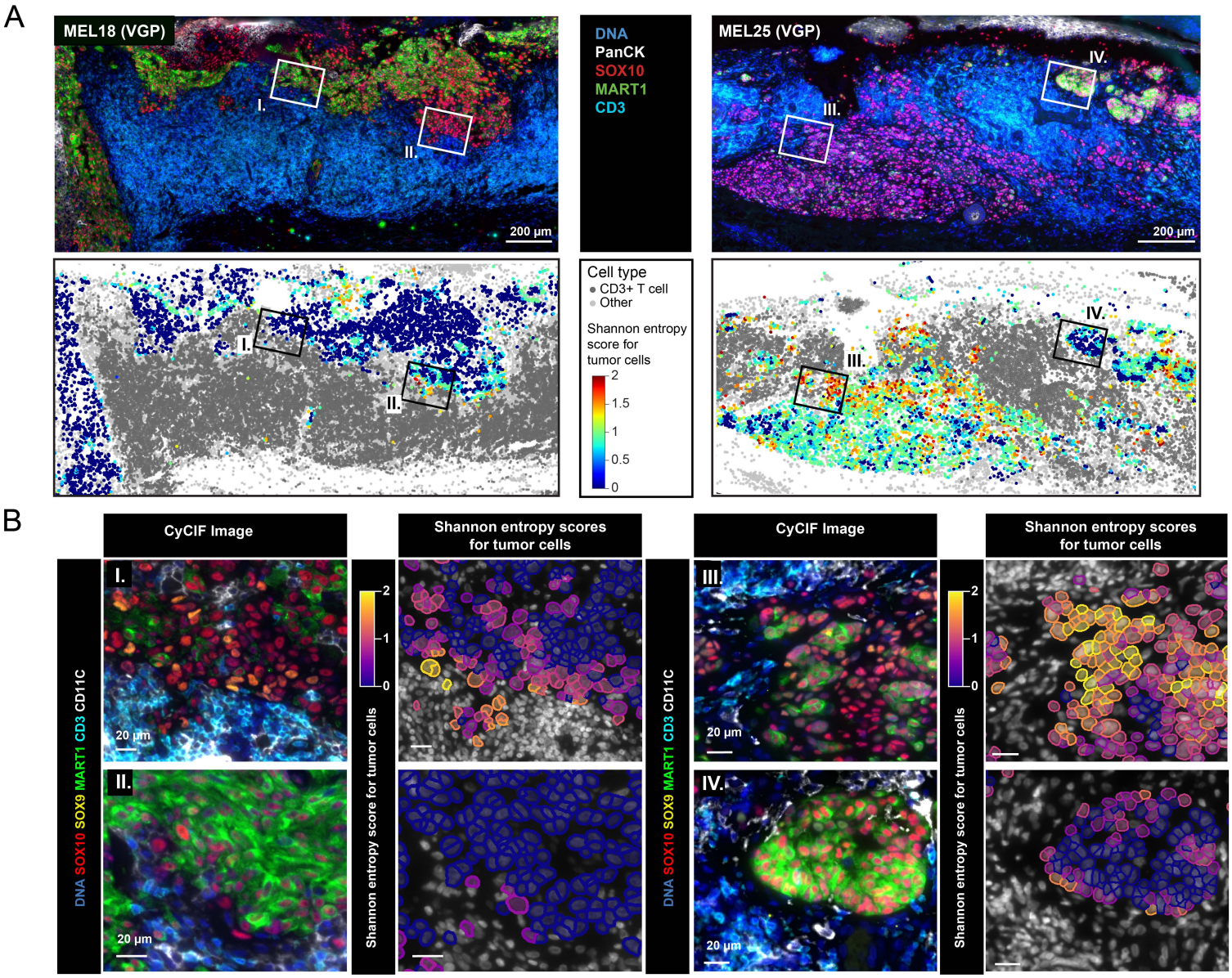
A
MEL18 (VGP)
I.
II.
200 µm
DNA
PanCK
SOX10
MART1
CD3
MEL25 (VGP)
III.
IV.
200 µm
Cell type
CD3+ T cell
Other
Shannon entropy score for tumor cells
2
1.5
1
0.5
0
B
CyCIF Image
Shannon entropy scores for tumor cells
DNA SOX10 SOX9 MART1 CD3 CD11C
Shannon entropy score for tumor cells
20 µm

941 **Figure 7. Quantifying tumor cell state heterogeneity with spatial entropy**

942 **A.** Top: CyCIF image of specimens MEL18 (top left) and MEL25 (top right) stained for DNA (blue),
943 epidermis (panCK; white), melanocytes (SOX10; red), tumor (MART1; green) and T cells (CD3; cyan).
944 Bottom: Scatter plots show the local neighborhood Shannon entropy values of each $SOX10^{+}$ tumor cell in
945 specimens MEL18 and MEL25, which are mapped back to the corresponding tissue location using the
946 X,Y coordinates of the cell centroids. Each data point represents a cell centroid. The centroids for CD3+
947 T cells and other non-tumor cells are shown with dark and light grey dots, respectively. The boxes
948 labeled as I-IV represent the regions magnified in **B**. Scale bars 200 μm. **B.** Magnified CyCIF ROIs from
949 **A**, stained for DNA (blue), SOX10 (red), MART1 (green), SOX9 (yellow), CD3 (cyan), CD11c (white). The
950 adjacent plots showing segmented tumor cells show the local neighborhood Shannon entropy values
951 calculated for each SOX10+ tumor cell within the magnified regions. Scale bars 20 μm.

Figure 8.

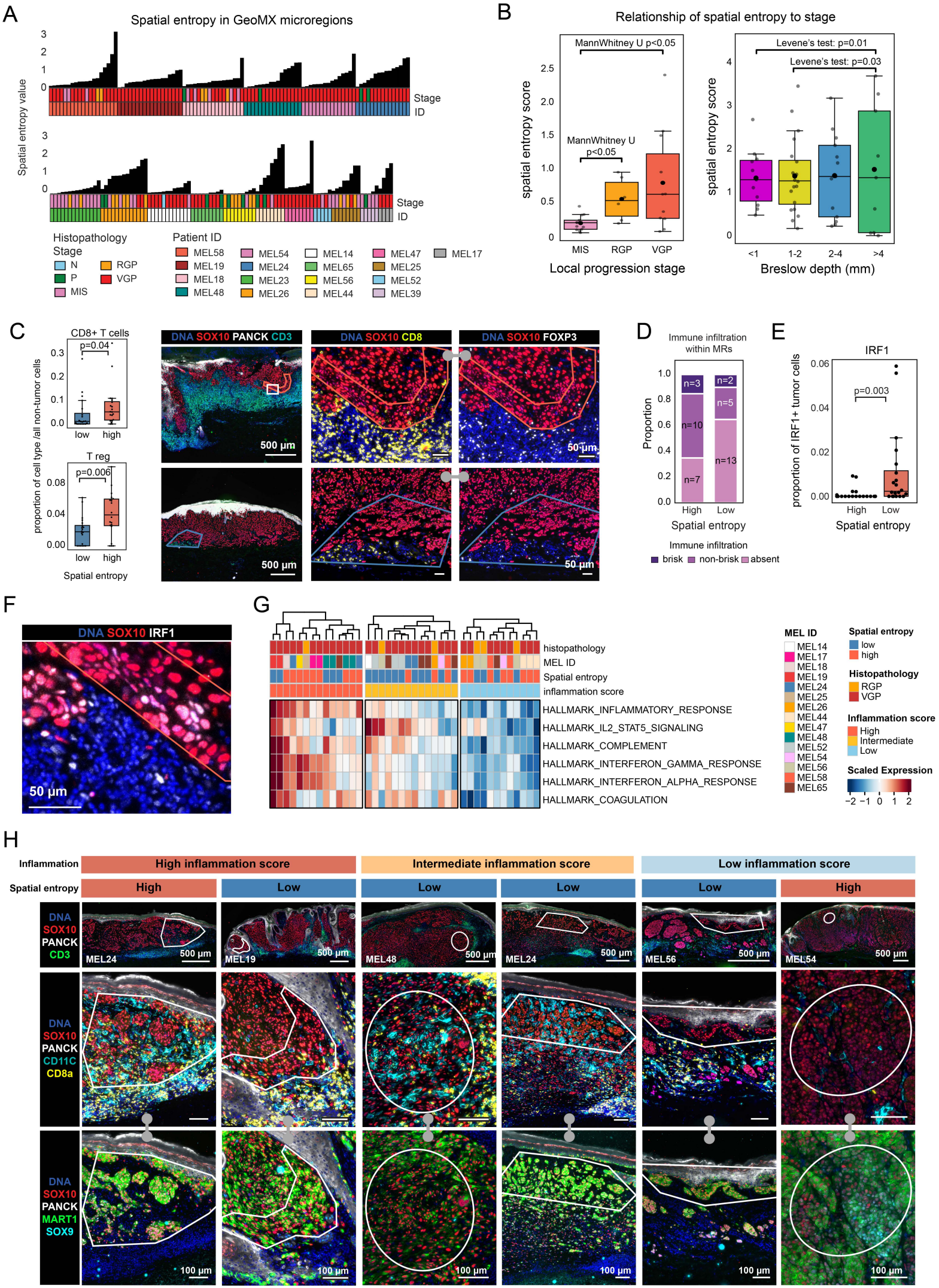
A
Spatial entropy in GeoMX microregions
Spatial entropy value
Stage
ID
Histopathology
Stage
N
P
MIS
RGP
VGP
Patient ID
MEL58
MEL19
MEL18
MEL48
MEL54
MEL24
MEL23
MEL26
MEL14
MEL65
MEL56
MEL44
MEL47
MEL25
MEL52
MEL39
MEL17
B
Relationship of spatial entropy to stage
MannWhitney U p<0.05
MannWhitney U p<0.05
spatial entropy score
MIS
RGP
VGP
Local progression stage
Levene's test: p=0.01
Levene's test: p=0.03
<1
1-2
2-4
>4
Breslow depth (mm)
C
CD8+ T cells
p=0.04
T reg
p=0.006
proportion of cell type /all non-tumor cells
low
high
Spatial entropy
DNA SOX10 PANCK CD3
DNA SOX10 CD8
DNA SOX10 FOXP3
500 µm
50 µm
D
Immune infiltration within MRs
Proportion
n=3
n=10
n=7
n=2
n=5
n=13
High
Low
Spatial entropy
Immune infiltration
brisk
non-brisk
absent
E
IRF1
p=0.003
proportion of IRF1+ tumor cells
High
Low
Spatial entropy
F
DNA SOX10 IRF1
50 µm
G
histopathology
MEL ID
Spatial entropy
inflammation score
HALLMARK_INFLAMMATORY_RESPONSE
HALLMARK_IL2_STAT5_SIGNALING
HALLMARK_COMPLEMENT
HALLMARK_INTERFERON_GAMMA_RESPONSE
HALLMARK_INTERFERON_ALPHA_RESPONSE
HALLMARK_COAGULATION
MEL ID
MEL14
MEL17
MEL18
MEL19
MEL24
MEL25
MEL26
MEL44
MEL47
MEL48
MEL52
MEL54
MEL56
MEL58
MEL65
Spatial entropy
low
high
Histopathology
RGP
VGP
Inflammation score
High
Intermediate
Low
Scaled Expression
−2 −1 0 1 2
H
Inflammation
High inflammation score
Intermediate inflammation score
Low inflammation score
Spatial entropy
High
Low
Low
Low
Low
High
DNA
SOX10
PANCK
CD3
MEL24
MEL19
MEL48
MEL24
MEL56
MEL54
500 µm
DNA
SOX10
PANCK
CD11C
CD8a
DNA
SOX10
PANCK
MART1
SOX9
100 µm

953 **Figure 8. Spatial entropy and inflammation.**

954 **A.** CoMut plot of the spatial entropy scores for each GeoMx microregion (MRs), calculated using CyCIF
955 data of the adjacent tissue section. Each MR is annotated for histopathology (N, P, MIS, RGP, VGP) and
956 patient ID. **B.** Spatial entropy scores calculated by local progression stages (left) and Breslow depth
957 (right; for RGP and VGP regions only). Each data point represents the spatial entropy score calculated
958 for a histologic region in a single sample. Box represents the first and third interquartiles of the data and
959 whiskers extend to show the rest of the distribution except for points that are determined to be outliers.
960 The p-value of local progression stage comparison was calculated using MannWhitney U test. The p-
961 value of Breslow depth comparison was calculated based on Levene's test. **C.** Left: The proportion of
962 $CD8^+$ T cells (top) and T regs (bottom) out of all non-tumor cells within high or low entropy microregions.
963 Each data point represents a mean cell type proportion within a single GeoMx MR, and the samples are
964 grouped by the MR spatial entropy scores. Box represents the first and third interquartiles of the data,
965 whiskers extend to show the rest of the distribution except for points that were determined to be outliers.
966 Right: CyCIF images of samples MEL18 (top), and MEL65 (bottom), stained for DNA (blue), panCK
967 (white) and SOX10 (red), CD3 (cyan). The magnified box in specimen MEL18 indicates a microregion
968 with high spatial entropy, and in specimen MEL65 indicates microregion with low spatial entropy. These
969 regions are magnified next to the whole-slide images and stained for DNA (blue), SOX10 (red), CD8
970 (yellow) and FOXP3 (white). Scale bars, 500 μm and 50 μm. **D.** Stacked bar plot showing the distribution
971 of annotations for immune cell infiltration as evaluated by CD45 staining for GeoMx MRs. The proportion
972 of various immune cell infiltration patterns is shown for MRs with high and low spatial entropy. The p-
973 value was calculated using Chi-square test. **E.** Boxplot showing the proportion of $IRF1^+$ tumor cells within
974 high and low entropy MRs. Each data point represents the mean proportion of marker+ cells within a
975 single GeoMx MR, and the samples are grouped by the MR spatial entropy scores. The p-value was
976 calculated using MannWhitney U test. **F.** Magnified field of view of a high spatial entropy MR shown in
977 panel **C** (specimen MEL18), stained for DNA (blue), IRF1 (white) and SOX10 (red). Scale bar, 50 μm. **G.**
978 The enrichment scores of Hallmark gene set (pathways) for spatial entropy MRs (n = 40), annotated by
979 histopathology (RGP, VGP), spatial entropy score grouping (high, low), patient ID, and inflammation
980 score (high, intermediate, low). **H.** Top row from left to right: CyCIF images of samples MEL24, MEL19,
981 MEL48, MEL24, MEL56 and MEL54, stained for DNA (blue), panCK (white), SOX10 (red), and CD3
982 (green). White regions indicate individual exemplary GeoMx MRs annotated for inflammation score and
983 spatial entropy (annotations shown on top of each column). These regions are magnified below the low
984 power fields of view and stained for DNA (blue), SOX10 (red), MART1 (green), CD3 (yellow) and CD11C
985 (cyan; middle row); DNA (blue), SOX10 (red), SOX9 (cyan), and MART1 (green; bottom row). Scale bars,
986 500 μm and 100 μm.

REFERENCES

(1) Domingues, B.; Lopes, J. M.; Soares, P.; Pópulo, H. Melanoma Treatment in Review. *ImmunoTargets Ther.* **2018**, *7*, 35–49. https://doi.org/10.2147/ITT.S134842.

(2) Arnold, M.; Singh, D.; Laversanne, M.; Vignat, J.; Vaccarella, S.; Meheus, F.; Cust, A. E.; de Vries, E.; Whiteman, D. C.; Bray, F. Global Burden of Cutaneous Melanoma in 2020 and Projections to 2040. *JAMA Dermatol.* **2022**, *158* (5), 495–503. https://doi.org/10.1001/jamadermatol.2022.0160.

(3) Watts, C. G.; McLoughlin, K.; Goumas, C.; van Kemenade, C. H.; Aitken, J. F.; Soyer, H. P.; Fernandez Peñas, P.; Guitera, P.; Scolyer, R. A.; Morton, R. L.; Menzies, S. W.; Caruana, M.; Kang, Y. J.; Mann, G. J.; Chakera, A. H.; Madronio, C. M.; Armstrong, B. K.; Thompson, J. F.; Cust, A. E. Association Between Melanoma Detected During Routine Skin Checks and Mortality. *JAMA Dermatol.* **2021**, *157* (12), 1–12. https://doi.org/10.1001/jamadermatol.2021.3884.

(4) Keung, E. Z.; Gershenwald, J. E. The Eighth Edition American Joint Committee on Cancer (AJCC) Melanoma Staging System: Implications for Melanoma Treatment and Care. *Expert Rev. Anticancer Ther.* **2018**, *18* (8), 775–784. https://doi.org/10.1080/14737140.2018.1489246.

(5) Lo, S. N.; Scolyer, R. A.; Thompson, J. F. Long-Term Survival of Patients with Thin (T1) Cutaneous Melanomas: A Breslow Thickness Cut Point of 0.8 Mm Separates Higher-Risk and Lower-Risk Tumors. *Ann. Surg. Oncol.* **2018**, *25* (4), 894–902. https://doi.org/10.1245/s10434-017-6325-1.

(6) Nielsen, J. B.; Kristiansen, I. S.; Thapa, S. Increasing Melanoma Incidence with Unchanged Mortality: More Sunshine, Better Treatment, Increased Diagnostic Activity, Overdiagnosis or Lowered Diagnostic Threshold? *Br. J. Dermatol.* **2024**, *191* (3), 365–374. https://doi.org/10.1093/bjd/ljae175.

(7) Shain, A. H.; Yeh, I.; Kovalyshyn, I.; Sriharan, A.; Talevich, E.; Gagnon, A.; Dummer, R.; North, J.; Pincus, L.; Ruben, B.; Rickaby, W.; D'Arrigo, C.; Robson, A.; Bastian, B. C. The Genetic Evolution of Melanoma from Precursor Lesions. *N. Engl. J. Med.* **2015**, *373* (20), 1926–1936. https://doi.org/10.1056/NEJMoa1502583.

(8) Tang, J.; Fewings, E.; Chang, D.; Zeng, H.; Liu, S.; Jorapur, A.; Belote, R. L.; McNeal, A. S.; Tan, T. M.; Yeh, I.; Arron, S. T.; Judson-Torres, R. L.; Bastian, B. C.; Shain, A. H. The Genomic Landscapes of Individual Melanocytes from Human Skin. *Nature* **2020**, *586* (7830), 600–605. https://doi.org/10.1038/s41586-020-2785-8.

(9) Curtin, J. A.; Fridlyand, J.; Kageshita, T.; Patel, H. N.; Busam, K. J.; Kutzner, H.; Cho, K.-H.; Aiba, S.; Bröcker, E.-B.; LeBoit, P. E.; Pinkel, D.; Bastian, B. C. Distinct Sets of Genetic Alterations in Melanoma. *N. Engl. J. Med.* **2005**, *353* (20), 2135–2147. https://doi.org/10.1056/NEJMoa050092.

(10) Galassi, C.; Chan, T. A.; Vitale, I.; Galluzzi, L. The Hallmarks of Cancer Immune Evasion. *Cancer Cell* **2024**, *42* (11), 1825–1863. https://doi.org/10.1016/j.ccell.2024.09.010.

(11) Rambow, F.; Marine, J.-C.; Goding, C. R. Melanoma Plasticity and Phenotypic Diversity: Therapeutic Barriers and Opportunities. *Genes Dev.* **2019**, *33* (19–20), 1295–1318. https://doi.org/10.1101/gad.329771.119.

(12) Nirmal, A. J.; Maliga, Z.; Vallius, T.; Quattrochi, B.; Chen, A. A.; Jacobson, C. A.; Pelletier, R. J.; Yapp, C.; Arias-Camison, R.; Chen, Y.-A.; Lian, C. G.; Murphy, G. F.; Santagata, S.; Sorger, P. K. The Spatial Landscape of Progression and Immunoediting in Primary Melanoma at Single-Cell Resolution. *Cancer Discov.* **2022**, *12* (6), 1518–1541. https://doi.org/10.1158/2159-8290.CD-21-1357.

(13) Tirosh, I.; Izar, B.; Prakadan, S. M.; Wadsworth, M. H.; Treacy, D.; Trombetta, J. J.; Rotem, A.; Rodman, C.; Lian, C.; Murphy, G.; Fallahi-Sichani, M.; Dutton-Regester, K.; Lin, J.-R.; Cohen, O.; Shah, P.; Lu, D.; Genshaft, A. S.; Hughes, T. K.; Ziegler, C. G. K.; Kazer, S. W.; Gaillard, A.; Kolb, K. E.; Villani, A.-C.; Johannessen, C. M.; Andreev, A. Y.; Van Allen, E. M.; Bertagnolli, M.; Sorger, P. K.; Sullivan, R. J.; Flaherty, K. T.; Frederick, D. T.; Jané-Valbuena, J.; Yoon, C. H.; Rozenblatt-Rosen, O.; Shalek, A. K.; Regev, A.; Garraway, L. A. Dissecting the Multicellular Ecosystem of Metastatic Melanoma by Single-Cell RNA-Seq. *Science* **2016**, *352* (6282), 189–196. https://doi.org/10.1126/science.aad0501.

(14) Biermann, J.; Melms, J. C.; Amin, A. D.; Wang, Y.; Caprio, L. A.; Karz, A.; Tagore, S.; Barrera, I.; Ibarra-Arellano, M. A.; Andreatta, M.; Fullerton, B. T.; Gretarsson, K. H.; Sahu, V.; Mangipudy, V. S.; Nguyen, T. T. T.; Nair, A.; Rogava, M.; Ho, P.; Koch, P. D.; Banu, M.; Humala, N.; Mahajan, A.; Walsh, Z. H.; Shah, S. B.; Vaccaro, D. H.; Caldwell, B.; Mu, M.; Wünnemann, F.; Chazotte, M.; Berhe, S.; Luoma, A. M.; Driver, J.; Ingham, M.; Khan, S. A.; Rapisuwon, S.; Slingluff, C. L.; Eigentler, T.; Röcken, M.; Carvajal, R.; Atkins, M. B.; Davies, M. A.; Agustinus, A.; Bakhoum, S. F.;

Azizi, E.; Siegelin, M.; Lu, C.; Carmona, S. J.; Hibshoosh, H.; Ribas, A.; Canoll, P.; Bruce, J. N.; Bi, W. L.; Agrawal, P.; Schapiro, D.; Hernando, E.; Macosko, E. Z.; Chen, F.; Schwartz, G. K.; Izar, B. Dissecting the Treatment-Naive Ecosystem of Human Melanoma Brain Metastasis. *Cell* **2022**, *185* (14), 2591-2608.e30. https://doi.org/10.1016/j.cell.2022.06.007.

(15) Liu, D.; Lin, J.-R.; Robitschek, E. J.; Kasumova, G. G.; Heyde, A.; Shi, A.; Kraya, A.; Zhang, G.; Moll, T.; Frederick, D. T.; Chen, Y.-A.; Wang, S.; Schapiro, D.; Ho, L.-L.; Bi, K.; Sahu, A.; Mei, S.; Miao, B.; Sharova, T.; Alvarez-Breckenridge, C.; Stocking, J. H.; Kim, T.; Fadden, R.; Lawrence, D.; Hoang, M. P.; Cahill, D. P.; Malehmir, M.; Nowak, M. A.; Brastianos, P. K.; Lian, C. G.; Ruppin, E.; Izar, B.; Herlyn, M.; Van Allen, E. M.; Nathanson, K.; Flaherty, K. T.; Sullivan, R. J.; Kellis, M.; Sorger, P. K.; Boland, G. M. Evolution of Delayed Resistance to Immunotherapy in a Melanoma Responder. *Nat. Med.* **2021**, *27* (6), 985–992. https://doi.org/10.1038/s41591-021-01331-8.

(16) Boshuizen, J.; Vredevoogd, D. W.; Krijgsman, O.; Ligtenberg, M. A.; Blankenstein, S.; De Bruijn, B.; Frederick, D. T.; Kenski, J. C. N.; Parren, M.; Brüggemann, M.; Madu, M. F.; Rozeman, E. A.; Song, J.-Y.; Horlings, H. M.; Blank, C. U.; Van Akkooi, A. C. J.; Flaherty, K. T.; Boland, G. M.; Peeper, D. S. Reversal of Pre-Existing NGFR-Driven Tumor and Immune Therapy Resistance. *Nat. Commun.* **2020**, *11* (1), 3946. https://doi.org/10.1038/s41467-020-17739-8.

(17) Widmer, D. S.; Cheng, P. F.; Eichhoff, O. M.; Belloni, B. C.; Zipser, M. C.; Schlegel, N. C.; Javelaud, D.; Mauviel, A.; Dummer, R.; Hoek, K. S. Systematic Classification of Melanoma Cells by Phenotype-specific Gene Expression Mapping. *Pigment Cell Melanoma Res.* **2012**, *25* (3), 343–353. https://doi.org/10.1111/j.1755-148X.2012.00986.x.

(18) Tsoi, J.; Robert, L.; Paraiso, K.; Galvan, C.; Sheu, K. M.; Lay, J.; Wong, D. J. L.; Atefi, M.; Shirazi, R.; Wang, X.; Braas, D.; Grasso, C. S.; Palaskas, N.; Ribas, A.; Graeber, T. G. Multi-Stage Differentiation Defines Melanoma Subtypes with Differential Vulnerability to Drug-Induced Iron-Dependent Oxidative Stress. *Cancer Cell* **2018**, *33* (5), 890-904.e5. https://doi.org/10.1016/j.ccell.2018.03.017.

(19) Hoek, K. S.; Schlegel, N. C.; Brafford, P.; Sucker, A.; Ugurel, S.; Kumar, R.; Weber, B. L.; Nathanson, K. L.; Phillips, D. J.; Herlyn, M.; Schadendorf, D.; Dummer, R. Metastatic Potential of Melanomas Defined by Specific Gene Expression Profiles with No BRAF Signature. *Pigment Cell Res.* **2006**, *19* (4), 290–302. https://doi.org/10.1111/j.1600-0749.2006.00322.x.

(20) Verfaillie, A.; Imrichova, H.; Atak, Z. K.; Dewaele, M.; Rambow, F.; Hulselmans, G.; Christiaens, V.; Svetlichnyy, D.; Luciani, F.; Van Den Mooter, L.; Claerhout, S.; Fiers, M.; Journe, F.; Ghanem, G.-E.; Herrmann, C.; Halder, G.; Marine, J.-C.; Aerts, S. Decoding the Regulatory Landscape of Melanoma Reveals TEADS as Regulators of the Invasive Cell State. *Nat. Commun.* **2015**, *6* (1), 6683. https://doi.org/10.1038/ncomms7683.

(21) Rambow, F.; Rogiers, A.; Marin-Bejar, O.; Aibar, S.; Femel, J.; Dewaele, M.; Karras, P.; Brown, D.; Chang, Y. H.; Debiec-Rychter, M.; Adriaens, C.; Radaelli, E.; Wolter, P.; Bechter, O.; Dummer, R.; Levesque, M.; Piris, A.; Frederick, D. T.; Boland, G.; Flaherty, K. T.; Van Den Oord, J.; Voet, T.; Aerts, S.; Lund, A. W.; Marine, J.-C. Toward Minimal Residual Disease-Directed Therapy in Melanoma. *Cell* **2018**, *174* (4), 843-855.e19. https://doi.org/10.1016/j.cell.2018.06.025.

(22) Hoek, K. S.; Eichhoff, O. M.; Schlegel, N. C.; Döbbeling, U.; Kobert, N.; Schaerer, L.; Hemmi, S.; Dummer, R. *In Vivo* Switching of Human Melanoma Cells between Proliferative and Invasive States. *Cancer Res.* **2008**, *68* (3), 650–656. https://doi.org/10.1158/0008-5472.CAN-07-2491.

(23) Wouters, J.; Kalender-Atak, Z.; Minnoye, L.; Spanier, K. I.; De Waegeneer, M.; Bravo González-Blas, C.; Mauduit, D.; Davie, K.; Hulselmans, G.; Najem, A.; Dewaele, M.; Pedri, D.; Rambow, F.; Makhzami, S.; Christiaens, V.; Ceyssens, F.; Ghanem, G.; Marine, J.-C.; Poovathingal, S.; Aerts, S. Robust Gene Expression Programs Underlie Recurrent Cell States and Phenotype Switching in Melanoma. *Nat. Cell Biol.* **2020**, *22* (8), 986–998. https://doi.org/10.1038/s41556-020-0547-3.

(24) Andrews, M. C.; Oba, J.; Wu, C.-J.; Zhu, H.; Karpinets, T.; Creasy, C. A.; Forget, M.-A.; Yu, X.; Song, X.; Mao, X.; Robertson, A. G.; Romano, G.; Li, P.; Burton, E. M.; Lu, Y.; Sloane, R. S.; Wani, K. M.; Rai, K.; Lazar, A. J.; Haydu, L. E.; Bustos, M. A.; Shen, J.; Chen, Y.; Morgan, M. B.; Wargo, J. A.; Kwong, L. N.; Haymaker, C. L.; Grimm, E. A.; Hwu, P.; Hoon, D. S. B.; Zhang, J.; Gershenwald, J. E.; Davies, M. A.; Futreal, P. A.; Bernatchez, C.; Woodman, S. E. Multi-Modal Molecular Programs Regulate Melanoma Cell State. *Nat. Commun.* **2022**, *13* (1), 4000. https://doi.org/10.1038/s41467-022-31510-1.

(25) Caramel, J.; Papadogeorgakis, E.; Hill, L.; Browne, G. J.; Richard, G.; Wierinckx, A.; Saldanha, G.; Osborne, J.; Hutchinson, P.; Tse, G.; Lachuer, J.; Puisieux, A.; Pringle, J. H.; Ansieau, S.;

Tulchinsky, E. A Switch in the Expression of Embryonic EMT-Inducers Drives the Development of Malignant Melanoma. *Cancer Cell* **2013**, *24* (4), 466–480. https://doi.org/10.1016/j.ccr.2013.08.018.

(26) Landsberg, J.; Kohlmeyer, J.; Renn, M.; Bald, T.; Rogava, M.; Cron, M.; Fatho, M.; Lennerz, V.; Wölfel, T.; Hölzel, M.; Tüting, T. Melanomas Resist T-Cell Therapy through Inflammation-Induced Reversible Dedifferentiation. *Nature* **2012**, *490* (7420), 412–416. https://doi.org/10.1038/nature11538.

(27) Kim, Y. J.; Sheu, K. M.; Tsoi, J.; Abril-Rodriguez, G.; Medina, E.; Grasso, C. S.; Torrejon, D. Y.; Champhekar, A. S.; Litchfield, K.; Swanton, C.; Speiser, D. E.; Scumpia, P. O.; Hoffmann, A.; Graeber, T. G.; Puig-Saus, C.; Ribas, A. Melanoma Dedifferentiation Induced by IFN-γ Epigenetic Remodeling in Response to Anti-PD-1 Therapy. *J. Clin. Invest.* **2021**, *131* (12), e145859, 145859. https://doi.org/10.1172/JCI145859.

(28) Widmer, D. S.; Hoek, K. S.; Cheng, P. F.; Eichhoff, O. M.; Biedermann, T.; Raaijmakers, M. I. G.; Hemmi, S.; Dummer, R.; Levesque, M. P. Hypoxia Contributes to Melanoma Heterogeneity by Triggering HIF1α-Dependent Phenotype Switching. *J. Invest. Dermatol.* **2013**, *133* (10), 2436–2443. https://doi.org/10.1038/jid.2013.115.

(29) Mehta, A.; Kim, Y. J.; Robert, L.; Tsoi, J.; Comin-Anduix, B.; Berent-Maoz, B.; Cochran, A. J.; Economou, J. S.; Tumeh, P. C.; Puig-Saus, C.; Ribas, A. Immunotherapy Resistance by Inflammation-Induced Dedifferentiation. *Cancer Discov.* **2018**, *8* (8), 935–943. https://doi.org/10.1158/2159-8290.CD-17-1178.

(30) Hoek, K. S.; Eichhoff, O. M.; Schlegel, N. C.; Döbbeling, U.; Kobert, N.; Schaerer, L.; Hemmi, S.; Dummer, R. *In Vivo* Switching of Human Melanoma Cells between Proliferative and Invasive States. *Cancer Res.* **2008**, *68* (3), 650–656. https://doi.org/10.1158/0008-5472.CAN-07-2491.

(31) Karras, P.; Bordeu, I.; Pozniak, J.; Nowosad, A.; Pazzi, C.; Van Raemdonck, N.; Landeloos, E.; Van Herck, Y.; Pedri, D.; Bervoets, G.; Makhzami, S.; Khoo, J. H.; Pavie, B.; Lamote, J.; Marin-Bejar, O.; Dewaele, M.; Liang, H.; Zhang, X.; Hua, Y.; Wouters, J.; Browaeys, R.; Bergers, G.; Saeys, Y.; Bosisio, F.; Van Den Oord, J.; Lambrechts, D.; Rustgi, A. K.; Bechter, O.; Blanpain, C.; Simons, B. D.; Rambow, F.; Marine, J.-C. A Cellular Hierarchy in Melanoma Uncouples Growth and Metastasis. *Nature* **2022**, *610* (7930), 190–198. https://doi.org/10.1038/s41586-022-05242-7.

(32) Pozniak, J.; Pedri, D.; Landeloos, E.; Van Herck, Y.; Antoranz, A.; Vanwynsberghe, L.; Nowosad, A.; Roda, N.; Makhzami, S.; Bervoets, G.; Maciel, L. F.; Pulido-Vicuña, C. A.; Pollaris, L.; Seurinck, R.; Zhao, F.; Flem-Karlsen, K.; Damsky, W.; Chen, L.; Karagianni, D.; Cinque, S.; Kint, S.; Vandereyken, K.; Rombaut, B.; Voet, T.; Vernaillen, F.; Annaert, W.; Lambrechts, D.; Boecxstaens, V.; Saeys, Y.; Van Den Oord, J.; Bosisio, F.; Karras, P.; Shain, A. H.; Bosenberg, M.; Leucci, E.; Paschen, A.; Rambow, F.; Bechter, O.; Marine, J.-C. A TCF4-Dependent Gene Regulatory Network Confers Resistance to Immunotherapy in Melanoma. *Cell* **2024**, *187* (1), 166-183.e25. https://doi.org/10.1016/j.cell.2023.11.037.

(33) Jerby-Arnon, L.; Shah, P.; Cuoco, M. S.; Rodman, C.; Su, M.-J.; Melms, J. C.; Leeson, R.; Kanodia, A.; Mei, S.; Lin, J.-R.; Wang, S.; Rabasha, B.; Liu, D.; Zhang, G.; Margolais, C.; Ashenberg, O.; Ott, P. A.; Buchbinder, E. I.; Haq, R.; Hodi, F. S.; Boland, G. M.; Sullivan, R. J.; Frederick, D. T.; Miao, B.; Moll, T.; Flaherty, K. T.; Herlyn, M.; Jenkins, R. W.; Thummalapalli, R.; Kowalczyk, M. S.; Cañadas, I.; Schilling, B.; Cartwright, A. N. R.; Luoma, A. M.; Malu, S.; Hwu, P.; Bernatchez, C.; Forget, M.-A.; Barbie, D. A.; Shalek, A. K.; Tirosh, I.; Sorger, P. K.; Wucherpfennig, K.; Van Allen, E. M.; Schadendorf, D.; Johnson, B. E.; Rotem, A.; Rozenblatt-Rosen, O.; Garraway, L. A.; Yoon, C. H.; Izar, B.; Regev, A. A Cancer Cell Program Promotes T Cell Exclusion and Resistance to Checkpoint Blockade. *Cell* **2018**, *175* (4), 984-997.e24. https://doi.org/10.1016/j.cell.2018.09.006.

(34) Ohsie, S. J.; Sarantopoulos, G. P.; Cochran, A. J.; Binder, S. W. Immunohistochemical Characteristics of Melanoma. *J. Cutan. Pathol.* **2008**, *35* (5), 433–444. https://doi.org/10.1111/j.1600-0560.2007.00891.x.

(35) Kim, R. H.; Meehan, S. A. Immunostain Use in the Diagnosis of Melanomas Referred to a Tertiary Medical Center: A 15-year Retrospective Review (2001–2015). *J. Cutan. Pathol.* **2017**, *44* (3), 221–227. https://doi.org/10.1111/cup.12867.

(36) Berset, M.; Cerottini, J. P.; Guggisberg, D.; Romero, P.; Burri, F.; Rimoldi, D.; Panizzon, R. G. Expression of Melan-A/MART-1 Antigen as a Prognostic Factor in Primary Cutaneous Melanoma. *Int. J. Cancer* **2001**, *95* (1), 73–77. https://doi.org/10.1002/1097-0215(20010120)95:1%253C73::aid-ijc1013%253E3.0.co;2-s.

(37) Laga, A. C.; Murphy, G. F. Cellular Heterogeneity in Vertical Growth Phase Melanoma. *Arch. Pathol. Lab. Med.* **2010**, *134* (12), 1750–1757. https://doi.org/10.5858/2009-0394-RAR.1.

(38) Hoashi, T.; Watabe, H.; Muller, J.; Yamaguchi, Y.; Vieira, W. D.; Hearing, V. J. MART-1 Is Required for the Function of the Melanosomal Matrix Protein PMEL17/GP100 and the Maturation of Melanosomes. *J. Biol. Chem.* **2005**, *280* (14), 14006–14016. https://doi.org/10.1074/jbc.M413692200.

(39) Kapur, R. P.; Bigler, S. A.; Skelly, M.; Gown, A. M. Anti-Melanoma Monoclonal Antibody HMB45 Identifies an Oncofetal Glycoconjugate Associated with Immature Melanosomes. *J. Histochem. Cytochem.* **1992**, *40* (2), 207–212. https://doi.org/10.1177/40.2.1552165.

(40) Cronin, J. C.; Watkins-Chow, D. E.; Incao, A.; Hasskamp, J. H.; Schönewolf, N.; Aoude, L. G.; Hayward, N. K.; Bastian, B. C.; Dummer, R.; Loftus, S. K.; Pavan, W. J. SOX10 Ablation Arrests Cell Cycle, Induces Senescence, and Suppresses Melanomagenesis. *Cancer Res.* **2013**, *73* (18), 5709–5718. https://doi.org/10.1158/0008-5472.CAN-12-4620.

(41) Gershenwald, J. E.; Scolyer, R. A.; Hess, K. R.; Sondak, V. K.; Long, G. V.; Ross, M. I.; Lazar, A. J.; Faries, M. B.; Kirkwood, J. M.; McArthur, G. A.; Haydu, L. E.; Eggermont, A. M. M.; Flaherty, K. T.; Balch, C. M.; Thompson, J. F.; for members of the American Joint Committee on Cancer Melanoma Expert Panel and the International Melanoma Database and Discovery Platform. Melanoma Staging: Evidence-based Changes in the American Joint Committee on Cancer Eighth Edition Cancer Staging Manual. *CA. Cancer J. Clin.* **2017**, *67* (6), 472–492. https://doi.org/10.3322/caac.21409.

(42) Clark, W. H.; From, L.; Bernardino, E. A.; Mihm, M. C. The Histogenesis and Biologic Behavior of Primary Human Malignant Melanomas of the Skin. *Cancer Res.* **1969**, *29* (3), 705–727.

(43) Maibach, F.; Sadozai, H.; Seyed Jafari, S. M.; Hunger, R. E.; Schenk, M. Tumor-Infiltrating Lymphocytes and Their Prognostic Value in Cutaneous Melanoma. *Front. Immunol.* **2020**, *11*. https://doi.org/10.3389/fimmu.2020.02105.

(44) Method of the Year 2024: Spatial Proteomics. *Nat. Methods* **2024**, *21* (12), 2195–2196. https://doi.org/10.1038/s41592-024-02565-3.

(45) Yapp, C.; Nirmal, A. J.; Zhou, F. Y.; Wong, A. Y. H.; Tefft, J.; Lu, Y. D.; Shang, Z.; Maliga, Z.; Llopis, P. M.; Murphy, G. F.; Lian, C.; Danuser, G.; Santagata, S.; Sorger, P. K. Highly Multiplexed 3D Profiling of Cell States and Immune Niches in Human Tumours. bioRxiv April 11, 2025, p 2023.11.10.566670. https://doi.org/10.1101/2023.11.10.566670.

(46) Ennen, M.; Keime, C.; Gambi, G.; Kieny, A.; Coassolo, S.; Thibault-Carpentier, C.; Margerin-Schaller, F.; Davidson, G.; Vagne, C.; Lipsker, D.; Davidson, I. *MITF* -High and *MITF* -Low Cells and a Novel Subpopulation Expressing Genes of Both Cell States Contribute to Intra- and Intertumoral Heterogeneity of Primary Melanoma. *Clin. Cancer Res.* **2017**, *23* (22), 7097–7107. https://doi.org/10.1158/1078-0432.CCR-17-0010.

(47) Kunz, M.; Löffler-Wirth, H.; Dannemann, M.; Willscher, E.; Doose, G.; Kelso, J.; Kottek, T.; Nickel, B.; Hopp, L.; Landsberg, J.; Hoffmann, S.; Tüting, T.; Zigrino, P.; Mauch, C.; Utikal, J.; Ziemer, M.; Schulze, H.-J.; Hölzel, M.; Roesch, A.; Kneitz, S.; Meierjohann, S.; Bosserhoff, A.; Binder, H.; Schartl, M. RNA-Seq Analysis Identifies Different Transcriptomic Types and Developmental Trajectories of Primary Melanomas. *Oncogene* **2018**, *37* (47), 6136–6151. https://doi.org/10.1038/s41388-018-0385-y.

(48) Kumar, S.; Warrell, J.; Li, S.; McGillivray, P. D.; Meyerson, W.; Salichos, L.; Harmanci, A.; Martinez-Fundichely, A.; Chan, C. W. Y.; Nielsen, M. M.; Lochovsky, L.; Zhang, Y.; Li, X.; Lou, S.; Pedersen, J. S.; Herrmann, C.; Getz, G.; Khurana, E.; Gerstein, M. B. Passenger Mutations in More Than 2,500 Cancer Genomes: Overall Molecular Functional Impact and Consequences. *Cell* **2020**, *180* (5), 915-927.e16. https://doi.org/10.1016/j.cell.2020.01.032.

(49) Lin, J.-R.; Izar, B.; Wang, S.; Yapp, C.; Mei, S.; Shah, P. M.; Santagata, S.; Sorger, P. K. Highly Multiplexed Immunofluorescence Imaging of Human Tissues and Tumors Using T-CyCIF and Conventional Optical Microscopes. *eLife* **2018**, *7*, e31657. https://doi.org/10.7554/eLife.31657.

(50) Zollinger, D. R.; Lingle, S. E.; Sorg, K.; Beechem, J. M.; Merritt, C. R. GeoMx™ RNA Assay: High Multiplex, Digital, Spatial Analysis of RNA in FFPE Tissue. *Methods Mol. Biol. Clifton NJ* **2020**, *2148*, 331–345. https://doi.org/10.1007/978-1-0716-0623-0_21.

(51) Elder, D. E. Melanoma Progression. *Pathology (Phila.)* **2016**, *48* (2), 147–154. https://doi.org/10.1016/j.pathol.2015.12.002.

(52) Pampena, R.; Kyrgidis, A.; Lallas, A.; Moscarella, E.; Argenziano, G.; Longo, C. A Meta-Analysis of Nevus-Associated Melanoma: Prevalence and Practical Implications. *J. Am. Acad. Dermatol.* **2017**, *77* (5), 938-945.e4. https://doi.org/10.1016/j.jaad.2017.06.149.

(53) Duffy, K.; Grossman, D. The Dysplastic Nevus: From Historical Perspective to Management in the Modern Era: Part I. Historical, Histologic, and Clinical Aspects. *J. Am. Acad. Dermatol.* **2012**, *67* (1), 1.e1-16; quiz 17–18. https://doi.org/10.1016/j.jaad.2012.02.047.
(54) Mata, D. A.; Lian, C. G.; Hafeez, F. Determining the Association Between Melanomas and Fields of Melanocytic Dysplasia. *Am. J. Dermatopathol.* **2022**, *45* (2), 90–92. https://doi.org/10.1097/dad.0000000000002339.
(55) Lian, C. G.; Murphy, G. F. The Genetic Evolution of Melanoma. *N. Engl. J. Med.* **2016**, *374* (10), 994–995. https://doi.org/10.1056/NEJMc1515834.
(56) Lin, J.-R.; Wang, S.; Coy, S.; Chen, Y.-A.; Yapp, C.; Tyler, M.; Nariya, M. K.; Heiser, C. N.; Lau, K. S.; Santagata, S.; Sorger, P. K. Multiplexed 3D Atlas of State Transitions and Immune Interaction in Colorectal Cancer. *Cell* **2023**, *186* (2), 363-381.e19. https://doi.org/10.1016/j.cell.2022.12.028.
(57) Baker, G. J.; Novikov, E.; Zhao, Z.; Vallius, T.; Davis, J. A.; Lin, J.-R.; Muhlich, J. L.; Mittendorf, E. A.; Santagata, S.; Guerriero, J. L.; Sorger, P. K. Quality Control for Single-Cell Analysis of High-Plex Tissue Profiles Using CyLinter. *Nat. Methods* **2024**, *21* (12), 2248–2259. https://doi.org/10.1038/s41592-024-02328-0.
(58) Schapiro, D.; Sokolov, A.; Yapp, C.; Chen, Y.-A.; Muhlich, J. L.; Hess, J.; Creason, A. L.; Nirmal, A. J.; Baker, G. J.; Nariya, M. K.; Lin, J.-R.; Maliga, Z.; Jacobson, C. A.; Hodgman, M. W.; Ruokonen, J.; Farhi, S. L.; Abbondanza, D.; McKinley, E. T.; Persson, D.; Betts, C.; Sivagnanam, S.; Regev, A.; Goecks, J.; Coffey, R. J.; Coussens, L. M.; Santagata, S.; Sorger, P. K. MCMICRO: A Scalable, Modular Image-Processing Pipeline for Multiplexed Tissue Imaging. *Nat. Methods* **2022**, *19* (3), 311–315. https://doi.org/10.1038/s41592-021-01308-y.
(59) Jönsson, G.; Busch, C.; Knappskog, S.; Geisler, J.; Miletic, H.; Ringnér, M.; Lillehaug, J. R.; Borg, Å.; Lønning, P. E. Gene Expression Profiling–Based Identification of Molecular Subtypes in Stage IV Melanomas with Different Clinical Outcome. *Clin. Cancer Res.* **2010**, *16* (13), 3356–3367. https://doi.org/10.1158/1078-0432.CCR-09-2509.
(60) Harbst, K.; Staaf, J.; Lauss, M.; Karlsson, A.; Måsbäck, A.; Johansson, I.; Bendahl, P.-O.; Vallon-Christersson, J.; Törngren, T.; Ekedahl, H.; Geisler, J.; Höglund, M.; Ringnér, M.; Lundgren, L.; Jirström, K.; Olsson, H.; Ingvar, C.; Borg, Å.; Tsao, H.; Jönsson, G. Molecular Profiling Reveals Low- and High-Grade Forms of Primary Melanoma. *Clin. Cancer Res.* **2012**, *18* (15), 4026–4036. https://doi.org/10.1158/1078-0432.CCR-12-0343.
(61) Thompson, J. F.; Soong, S.-J.; Balch, C. M.; Gershenwald, J. E.; Ding, S.; Coit, D. G.; Flaherty, K. T.; Gimotty, P. A.; Johnson, T.; Johnson, M. M.; Leong, S. P.; Ross, M. I.; Byrd, D. R.; Cascinelli, N.; Cochran, A. J.; Eggermont, A. M.; McMasters, K. M.; Mihm, M. C.; Morton, D. L.; Sondak, V. K. Prognostic Significance of Mitotic Rate in Localized Primary Cutaneous Melanoma: An Analysis of Patients in the Multi-Institutional American Joint Committee on Cancer Melanoma Staging Database. *J. Clin. Oncol.* **2011**, *29* (16), 2199–2205. https://doi.org/10.1200/JCO.2010.31.5812.
(62) Gimotty, P. A.; Van Belle, P.; Elder, D. E.; Murry, T.; Montone, K. T.; Xu, X.; Hotz, S.; Raines, S.; Ming, M. E.; Wahl, P.; Guerry, D. Biologic and Prognostic Significance of Dermal Ki67 Expression, Mitoses, and Tumorigenicity in Thin Invasive Cutaneous Melanoma. *J. Clin. Oncol.* **2005**, *23* (31), 8048–8056. https://doi.org/10.1200/JCO.2005.02.0735.
(63) Du, J.; Miller, A. J.; Widlund, H. R.; Horstmann, M. A.; Ramaswamy, S.; Fisher, D. E. MLANA/MART1 and SILV/PMEL17/GP100 Are Transcriptionally Regulated by MITF in Melanocytes and Melanoma. *Am. J. Pathol.* **2003**, *163* (1), 333–343. https://doi.org/10.1016/S0002-9440(10)63657-7.
(64) Fetsch, P. A.; Marincola, F. M.; Filie, A.; Hijazi, Y. M.; Kleiner, D. E.; Abati, A. Melanoma-Associated Antigen Recognized by T Cells (MART-1): The Advent of a Preferred Immunocytochemical Antibody for the Diagnosis of Metastatic Malignant Melanoma with Fine-Needle Aspiration. *Cancer* **1999**, *87* (1), 37–42.
(65) Qiu, W.; Chuong, C.-M.; Lei, M. Regulation of Melanocyte Stem Cells in the Pigmentation of Skin and Its Appendages: Biological Patterning and Therapeutic Potentials. *Exp. Dermatol.* **2019**, *28* (4), 395–405. https://doi.org/10.1111/exd.13856.
(66) Vidal, A.; Redmer, T. Decoding the Role of CD271 in Melanoma. *Cancers* **2020**, *12* (9), 2460. https://doi.org/10.3390/cancers12092460.
(67) Gopalan, V.; Day, C.-P.; Pérez-Guijarro, E.; Chin, S.; Ebersole, J.; Smith, C.; Simpson, M.; Sassano, A.; Constantino, M. A.; Wu, E.; Yang, H. H.; Lee, M. P.; Hannenhalli, S.; Merlino, G.; Marie, K. L. *Comprehensive Single-Cell Transcriptomic Analysis of Embryonic Melanoblasts Uncovers Lineage-*

Specific Mechanisms of Melanoma Metastasis and Therapy Resistance; preprint; Cancer Biology, 2022. https://doi.org/10.1101/2022.10.14.512297.

(68) Yang, G.; Li, Y.; Nishimura, E. K.; Xin, H.; Zhou, A.; Guo, Y.; Dong, L.; Denning, M. F.; Nickoloff, B. J.; Cui, R. Inhibition of PAX3 by TGF-β Modulates Melanocyte Viability. *Mol. Cell* **2008**, *32* (4), 554–563. https://doi.org/10.1016/j.molcel.2008.11.002.

(69) Javelaud, D.; Alexaki, V.; Mauviel, A. Transforming Growth Factor-β in Cutaneous Melanoma. *Pigment Cell Melanoma Res.* **2008**, *21* (2), 123–132. https://doi.org/10.1111/j.1755-148X.2008.00450.x.

(70) Zhang, Z.; Imani, S.; Shasaltaneh, M. D.; Hosseinifard, H.; Zou, L.; Fan, Y.; Wen, Q. The Role of Vascular Mimicry as a Biomarker in Malignant Melanoma: A Systematic Review and Meta-Analysis. *BMC Cancer* **2019**, *19* (1), 1134. https://doi.org/10.1186/s12885-019-6350-5.

(71) Xu, Y.; Olman, V.; Xu, D. Minimum Spanning Trees for Gene Expression Data Clustering. *Genome Inform. Int. Conf. Genome Inform.* **2001**, *12*, 24–33.

(72) Hsu, M. Y.; Meier, F. E.; Nesbit, M.; Hsu, J. Y.; Van Belle, P.; Elder, D. E.; Herlyn, M. E-Cadherin Expression in Melanoma Cells Restores Keratinocyte-Mediated Growth Control and down-Regulates Expression of Invasion-Related Adhesion Receptors. *Am. J. Pathol.* **2000**, *156* (5), 1515–1525. https://doi.org/10.1016/S0002-9440(10)65023-7.

(73) Srivastava, A.; Laidler, P.; Davies, R. P.; Horgan, K.; Hughes, L. E. The Prognostic Significance of Tumor Vascularity in Intermediate-Thickness (0.76-4.0 Mm Thick) Skin Melanoma. A Quantitative Histologic Study. *Am. J. Pathol.* **1988**, *133* (2), 419–423.

(74) Centofanti, E.; Wang, C.; Iyer, S.; Krichevsky, O.; Oyler-Yaniv, A.; Oyler-Yaniv, J. The Spread of Interferon-γ in Melanomas Is Highly Spatially Confined, Driving Nongenetic Variability in Tumor Cells. *Proc. Natl. Acad. Sci. U. S. A.* **2023**, *120* (35), e2304190120. https://doi.org/10.1073/pnas.2304190120.

(75) Mihm, M. C.; Mulé, J. J. Reflections on the Histopathology of Tumor-Infiltrating Lymphocytes in Melanoma and the Host Immune Response. *Cancer Immunol. Res.* **2015**, *3* (8), 827–835. https://doi.org/10.1158/2326-6066.CIR-15-0143.

(76) Cugno, M.; Borghi, A.; Garcovich, S.; Marzano, A. V. Coagulation and Skin Autoimmunity. *Front. Immunol.* **2019**, *10*. https://doi.org/10.3389/fimmu.2019.01407.

(77) Hieken, T. J.; Kreidieh, F.; Aedo-Lopez, V.; Block, M. S.; McArthur, G. A.; Amaria, R. N. Neoadjuvant Immunotherapy in Melanoma: The Paradigm Shift. *Am. Soc. Clin. Oncol. Educ. Book* **2023**, No. 43, e390614. https://doi.org/10.1200/EDBK_390614.

(78) Bai, X.; Fisher, D. E.; Flaherty, K. T. Cell-State Dynamics and Therapeutic Resistance in Melanoma from the Perspective of MITF and IFNγ Pathways. *Nat. Rev. Clin. Oncol.* **2019**, *16* (9), 549–562. https://doi.org/10.1038/s41571-019-0204-6.

(79) Li, F. Z.; Dhillon, A. S.; Anderson, R. L.; McArthur, G.; Ferrao, P. T. Phenotype Switching in Melanoma: Implications for Progression and Therapy. *Front. Oncol.* **2015**, *5*, 31. https://doi.org/10.3389/fonc.2015.00031.

(80) Hölzel, M.; Tüting, T. Inflammation-Induced Plasticity in Melanoma Therapy and Metastasis. *Trends Immunol.* **2016**, *37* (6), 364–374. https://doi.org/10.1016/j.it.2016.03.009.

(81) Lugassy, C.; Kleinman, H. K.; Vermeulen, P. B.; Barnhill, R. L. Angiotropism, Pericytic Mimicry and Extravascular Migratory Metastasis: An Embryogenesis-Derived Program of Tumor Spread. *Angiogenesis* **2020**, *23* (1), 27–41. https://doi.org/10.1007/s10456-019-09695-9.

(82) Hunter, M. V.; Joshi, E.; Bowker, S.; Montal, E.; Ma, Y.; Kim, Y. H.; Yang, Z.; Tuffery, L.; Li, Z.; Rosiek, E.; Browning, A.; Moncada, R.; Yanai, I.; Byrne, H.; Monetti, M.; de Stanchina, E.; Hamard, P.-J.; Koche, R. P.; White, R. M. Mechanical Confinement Governs Phenotypic Plasticity in Melanoma. *Nature* **2025**, *647* (8089), 517–527. https://doi.org/10.1038/s41586-025-09445-6.

(83) McConnell, A. M.; Chassé, M. H.; Noonan, H. R.; Mito, J. K.; Weiskopf, E.; Gosselink, I. F.; Prasad, M.; Yang, S.; Abarzua, P.; Lian, C. G.; Murphy, G. F.; Trapnell, C.; Zon, L. I. *An Attractor State Zone Precedes Neural Crest Fate in Melanoma Initiation*; Cold Spring Harbor Laboratory, 2024. https://doi.org/10.1101/2024.10.22.618007.

(84) Chu, X.; Tian, W.; Ning, J.; Xiao, G.; Zhou, Y.; Wang, Z.; Zhai, Z.; Tanzhu, G.; Yang, J.; Zhou, R. Cancer Stem Cells: Advances in Knowledge and Implications for Cancer Therapy. *Signal Transduct. Target. Ther.* **2024**, *9*, 170. https://doi.org/10.1038/s41392-024-01851-y.

(85) Smith, M. P.; Sanchez-Laorden, B.; O'Brien, K.; Brunton, H.; Ferguson, J.; Young, H.; Dhomen, N.; Flaherty, K. T.; Frederick, D. T.; Cooper, Z. A.; Wargo, J. A.; Marais, R.; Wellbrock, C. The Immune

Microenvironment Confers Resistance to MAPK Pathway Inhibitors through Macrophage-Derived TNFα. *Cancer Discov.* **2014**, *4* (10), 1214–1229. https://doi.org/10.1158/2159-8290.CD-13-1007.

(86) Braverman, I. M. The Cutaneous Microcirculation. *J. Investig. Dermatol. Symp. Proc.* **2000**, *5* (1), 3–9. https://doi.org/10.1046/j.1087-0024.2000.00010.x.

(87) Balood, M.; Ahmadi, M.; Eichwald, T.; Ahmadi, A.; Majdoubi, A.; Roversi, K.; Roversi, K.; Lucido, C. T.; Restaino, A. C.; Huang, S.; Ji, L.; Huang, K.-C.; Semerena, E.; Thomas, S. C.; Trevino, A. E.; Merrison, H.; Parrin, A.; Doyle, B.; Vermeer, D. W.; Spanos, W. C.; Williamson, C. S.; Seehus, C. R.; Foster, S. L.; Dai, H.; Shu, C. J.; Rangachari, M.; Thibodeau, J.; V. Del Rincon, S.; Drapkin, R.; Rafei, M.; Ghasemlou, N.; Vermeer, P. D.; Woolf, C. J.; Talbot, S. Nociceptor Neurons Affect Cancer Immunosurveillance. *Nature* **2022**, *611* (7935), 405–412. https://doi.org/10.1038/s41586-022-05374-w.

(88) Pozdnyakova, O.; Grossman, J.; Barbagallo, B.; Lyle, S. The Hair Follicle Barrier to Involvement by Malignant Melanoma. *Cancer* **2009**, *115* (6), 1267–1275. https://doi.org/10.1002/cncr.24117.

(89) Grossman, D.; Okwundu, N.; Bartlett, E. K.; Marchetti, M. A.; Othus, M.; Coit, D. G.; Hartman, R. I.; Leachman, S. A.; Berry, E. G.; Korde, L.; Lee, S. J.; Bar-Eli, M.; Berwick, M.; Bowles, T.; Buchbinder, E. I.; Burton, E. M.; Chu, E. Y.; Curiel-Lewandrowski, C.; Curtis, J. A.; Daud, A.; Deacon, D. C.; Ferris, L. K.; Gershenwald, J. E.; Grossmann, K. F.; Hu-Lieskovan, S.; Hyngstrom, J.; Jeter, J. M.; Judson-Torres, R. L.; Kendra, K. L.; Kim, C. C.; Kirkwood, J. M.; Lawson, D. H.; Leming, P. D.; Long, G. V.; Marghoob, A. A.; Mehnert, J. M.; Ming, M. E.; Nelson, K. C.; Polsky, D.; Scolyer, R. A.; Smith, E. A.; Sondak, V. K.; Stark, M. S.; Stein, J. A.; Thompson, J. A.; Thompson, J. F.; Venna, S. S.; Wei, M. L.; Swetter, S. M. Prognostic Gene Expression Profiling in Cutaneous Melanoma: Identifying the Knowledge Gaps and Assessing the Clinical Benefit. *JAMA Dermatol.* **2020**, *156* (9), 1004. https://doi.org/10.1001/jamadermatol.2020.1729.

(90) Chan, W. H.; Tsao, H. Consensus, Controversy, and Conversations About Gene Expression Profiling in Melanoma. *JAMA Dermatol.* **2020**, *156* (9), 949–951. https://doi.org/10.1001/jamadermatol.2020.1730.

(91) Sun, J.; Karasaki, K. M.; Farma, J. M. The Use of Gene Expression Profiling and Biomarkers in Melanoma Diagnosis and Predicting Recurrence: Implications for Surveillance and Treatment. *Cancers* **2024**, *16* (3), 583. https://doi.org/10.3390/cancers16030583.

(92) Stassen, R. C.; Mulder, E. E. A. P.; Mooyaart, A. L.; Francken, A. B.; van der Hage, J.; Aarts, M. J. B.; van der Veldt, A. A. M.; Verhoef, C.; Grünhagen, D. J. Clinical Evaluation of the Clinicopathologic and Gene Expression Profile (CP-GEP) in Patients with Melanoma Eligible for Sentinel Lymph Node Biopsy: A Multicenter Prospective Dutch Study. *Eur. J. Surg. Oncol. J. Eur. Soc. Surg. Oncol. Br. Assoc. Surg. Oncol.* **2023**, *49* (12), 107249. https://doi.org/10.1016/j.ejso.2023.107249.

(93) Amaral, T.; Chatziioannou, E.; Nuebling, A.; Nanz, L.; Sinnberg, T.; Niessner, H.; Arentsen, T.; Ruiter, R.; Dwarkasing, J.; Eggermont, A. M.; Leiter, U.; Flatz, L.; Forchhammer, S. Risk Stratification Using the Merlin Assay (CP-GEP) in an Independent Cohort of 930 Patients with Clinical Stage I/II Melanoma Who Did Not Undergo Sentinel Lymph Node Biopsy. *Eur. J. Cancer* **2025**, *220*, 115372. https://doi.org/10.1016/j.ejca.2025.115372.

(94) Cook, R. W.; Middlebrook, B.; Wilkinson, J.; Covington, K. R.; Oelschlager, K.; Monzon, F. A.; Stone, J. F. Analytic Validity of DecisionDx-Melanoma, a Gene Expression Profile Test for Determining Metastatic Risk in Melanoma Patients. *Diagn. Pathol.* **2018**, *13* (1), 13. https://doi.org/10.1186/s13000-018-0690-3.

(95) Wan, G.; Nguyen, N.; Liu, F.; DeSimone, M. S.; Leung, B. W.; Rajeh, A.; Collier, M. R.; Choi, M. S.; Amadife, M.; Tang, K.; Zhang, S.; Phillipps, J. S.; Jairath, R.; Alexander, N. A.; Hua, Y.; Jiao, M.; Chen, W.; Ho, D.; Duey, S.; Németh, I. B.; Marko-Varga, G.; Valdés, J. G.; Liu, D.; Boland, G. M.; Gusev, A.; Sorger, P. K.; Yu, K.-H.; Semenov, Y. R. Prediction of Early-Stage Melanoma Recurrence Using Clinical and Histopathologic Features. *NPJ Precis. Oncol.* **2022**, *6* (1), 79. https://doi.org/10.1038/s41698-022-00321-4.

(96) Hoffer, J.; Rashid, R.; Muhlich, J.; Chen, Y.-A.; Russell, D.; Ruokonen, J.; Krueger, R.; Pfister, H.; Santagata, S.; Sorger, P. Minerva: A Light-Weight, Narrative Image Browser for Multiplexed Tissue Images. *J. Open Source Softw.* **2020**, *5* (54), 2579. https://doi.org/10.21105/joss.02579.

(97) Schapiro, D.; Yapp, C.; Sokolov, A.; Reynolds, S. M.; Chen, Y.-A.; Sudar, D.; Xie, Y.; Muhlich, J.; Arias-Camison, R.; Arena, S.; Taylor, A. J.; Nikolov, M.; Tyler, M.; Lin, J.-R.; Burlingame, E. A.; Human Tumor Atlas Network; Chang, Y. H.; Farhi, S. L.; Thorsson, V.; Venkatamohan, N.; Drewes, J. L.; Pe'er, D.; Gutman, D. A.; Herrmann, M. D.; Gehlenborg, N.; Bankhead, P.; Roland, J. T.; Herndon, J. M.; Snyder, M. P.; Angelo, M.; Nolan, G.; Swedlow, J. R.; Schultz, N.; Merrick, D. T.;

Mazzili, S. A.; Cerami, E.; Rodig, S. J.; Santagata, S.; Sorger, P. K. MITI Minimum Information Guidelines for Highly Multiplexed Tissue Images. *Nat. Methods* **2022**, *19* (3), 262–267. https://doi.org/10.1038/s41592-022-01415-4.

(98) Lin, J.-R.; Izar, B.; Wang, S.; Yapp, C.; Mei, S.; Shah, P. M.; Santagata, S.; Sorger, P. K. Highly Multiplexed Immunofluorescence Imaging of Human Tissues and Tumors Using T-CyCIF and Conventional Optical Microscopes. *eLife* **2018**, *7*, e31657. https://doi.org/10.7554/eLife.31657.

(99) Nirmal, A. J.; Sorger, P. K. SCIMAP: A Python Toolkit for Integrated SpatialAnalysis of Multiplexed Imaging Data. *J. Open Source Softw.* **2024**, *9* (97), 6604. https://doi.org/10.21105/joss.06604.

(100) Altieri, L.; Cocchi, D.; Roli, G. Efficient Computation of Spatial Entropy Measures. *Entropy* **2023**, *25* (12), 1634. https://doi.org/10.3390/e25121634.

(101) Batty, M.; Morphet, R.; Masucci, P.; Stanilov, K. Entropy, Complexity, and Spatial Information. *J. Geogr. Syst.* **2014**, *16* (4), 363–385. https://doi.org/10.1007/s10109-014-0202-2.

(102) Wang, C.; Zhao, H. Spatial Heterogeneity Analysis: Introducing a New Form of Spatial Entropy. *Entropy* **2018**, *20* (6), 398. https://doi.org/10.3390/e20060398.

(103) Wan, G.; Maliga, Z.; Yan, B.; Vallius, T.; Shi, Y.; Khattab, S.; Chang, C.; Nirmal, A. J.; Yu, K.-H.; Liu, D.; Lian, C. G.; DeSimone, M. S.; Sorger, P. K.; Semenov, Y. R. SpatialCells: Automated Profiling of Tumor Microenvironments with Spatially Resolved Multiplexed Single-Cell Data. *Brief. Bioinform.* **2024**, *25* (3), bbae189. https://doi.org/10.1093/bib/bbae189.

(104) Love, M. I.; Huber, W.; Anders, S. Moderated Estimation of Fold Change and Dispersion for RNA-Seq Data with DESeq2. *Genome Biol.* **2014**, *15* (12), 550. https://doi.org/10.1186/s13059-014-0550-8.

(105) Wirth, H.; Löffler, M.; Von Bergen, M.; Binder, H. Expression Cartography of Human Tissues Using Self Organizing Maps. *BMC Bioinformatics* **2011**, *12* (1), 306. https://doi.org/10.1186/1471-2105-12-306.

(106) Wirth, H.; Von Bergen, M.; Binder, H. Mining SOM Expression Portraits: Feature Selection and Integrating Concepts of Molecular Function. *BioData Min.* **2012**, *5* (1), 18. https://doi.org/10.1186/1756-0381-5-18.